Joint Centre for Mesoscale Meteorology, Reading, UK

Objective Fronts

T. D. Hewson

Internal Report No. 57

March 1996

Met Office Joint Centre for Mesoscale Meteorology Department of Meteorology
University of Reading PO Box 243 Reading RG6 6BB United Kingdom
Tel: +44 (0)118 931 8425 Fax: +44 (0)118 931 8791
www.metoffice.com

Designed and produced by the Met Office © Crown copyright 2001 01/0240 The Met Office logo is a registered trademark.

Objective Fronts

T. D. Hewson

address: Joint Centre for Mesoscale Meteorology, University of Reading, PO Box 240, Reading RG6 6FN, U.K.

email: tdhewson@meto.govt.uk, tel: 01734 316626, fax: 01734 318791

Abstract: This paper addresses the long-standing problem of plotting atmospheric fronts objectively. A thermodynamic definition of a front is proposed. Time-independent diagnostic quantities are then devised according to this definition. These can be computed from any gridded dataset. Fronts are then plotted, without human intervention, by utilising standard graphics package facilities, such as contouring, to represent the diagnostics. The methodology includes applying threshold criteria to automatically erase fronts which are thermally weak. By tuning these criteria a good match with subjective fronts is obtained. In addition, the objective surface fronts very often coincide with troughs in surface pressure, implying that a thermodynamic definition is sufficient. The objective front-plotting is further developed to recognise split fronts, and ana- and kata-front characteristics. Many examples are presented; these illustrate how objective fronts are potentially a very powerful tool for both forecasting and research. Here at JCMM plots and animations showing objective fronts have been produced on a daily basis for several months now.

The concept of atmospheric fronts was introduced by the Bergen school early in the 20th century (Bjerknes and Solberg (1922)). Since this pioneering work there have been phenomenal advances in computing and observational technology, and it is now possible to generate, with relative ease, fields of temperature, wind and other front-related variables, covering many spatial scales, either as objective analyses or numerical predictions. Yet in spite of these many advances there is still no widely accepted, *objective* method of recognising and plotting atmospheric fronts, even using computer-generated gridded datasets. In the last 15 years some 3600 paper abstracts have referred to fronts and frontal systems, and in most published work which touches on synoptic meteorology one will find at least one figure depicting them, but in the vast majority of cases frontal positioning will have been a subjective process.

One problem is that meteorologists are trained to recognise fronts, at least at the surface, on the basis of many parameters, such as temperature, wind shifts (vorticity), dewpoint, cloud cover, cloud types, visibility and lines in precipitation patterns, and that in routine numerical model output some of these are poorly represented. However, this argument against the use of model-based objective analysis obscures the fact that different forecasters/synopticians will frequently produce different frontal analyses from the same datasets (see Renard and Clarke (1965), Mass (1991) and Sanders (1995) for examples). The solution must be to generate objective fronts on the basis of fundamental variable(s) which *are* considered to be well handled by the models.

The potential uses of 'objective fronts' are numerous. In the forecasting environment considerable time and money would be saved by having available, at least as a first guess for subsequent modification, on-screen surface charts with fronts, for both analysis and forecast times. Model run comparisons, particularly in terms of timing and positioning, become more straightforward and intelligible when lines (i.e. fronts) from successive runs can be overlaid. In research readily-available objectively-defined fronts would facilitate the production of front and frontal wave climatologies, as well as provide a means for objectively assessing the utility of current conceptual models, and perhaps also developing others. Dynamical studies could also benefit greatly from placing emphasis on frontal zones. One important issue in current research, for example, concerns the development of frontal wave cyclones (see Thorpe (1994)). Are such cyclones most likely to develop on fronts where the upper level forcing is greatest, or is it some other parameter, such as the large scale deformation (see Bishop and Thorpe (1994)), which is more important? Important dynamical questions such as this would be very difficult to address routinely without the aid of an objective method of recognising fronts.

The purpose of this paper is thus to document a new, simple and accurate way of objectively identifying and plotting atmospheric fronts, which can be applied to any gridded dataset. The methodology blends together mathematical and graphical techniques to produce output in an attractive, compact and instructive format. Only *standard* graphics package facilities are used to actually plot the fronts, thus enhancing portability. Another advantage is that the new methodology is allied to a precise dynamical definition of a front, and as such requires no human intervention, unlike techniques found in many past publications.

The general methodology to be described can be applied to other meteorological features which are represented in a similar way - that is as 'lines of finite length'. Examples are jet streams, trough-lines and thermal troughs and ridges (the mathematics required to represent these quantities will be described in a brief follow-up paper). It seems likely that applications also exist in other scientific fields.

The layout of the paper is as follows: the main requirements of the objective technique are listed (section 1), and the term front then defined (section 2). Past work in the field is reviewed in section 3 and graphical considerations described in section 4. The new techniques themselves are covered in section 5, together with examples derived from operational model data. Section 6 details some enhancements to the general front-plotting methodology which facilitate, for example, the objective identification of ana-fronts and kata-fronts. Section 7 provides further examples of tailored output, whilst section 8 lists conclusions.

1. Aims

In developing an objective method of drawing fronts on a chart several key requirements were identified. Specifically, the objective technique should be:

i) Simple

The technique should be based on as few quantities, as little differentiation, and as small a number of grid points (in arriving at differentials) as possible. This should reduce complexity, reduce noise, and reduce the smoothing out of significant features in the initial fields.

ii) Intelligible

The way in which any differentiated quantities relate to the initial fields should be readily apparent.

iii) Accurate

A reasonable level of agreement with manual analyses is important, particularly for strong fronts. However, endeavouring to produce *exact* replicas would be futile. This is because manual analyses are generally not repeatable, and because analysts cannot help but be influenced by conceptual models of frontal structure and evolution, models which themselves evolve with time (see Shapiro and Keyser (1990)). Indeed objective fronts may intimate refinements to these models.

iv) Tuneable

A facility whereby fronts were not plotted unless they reached some 'threshold intensity' criteria would be advantageous. Alternatively fronts could be displayed in different ways according to 'intensity'.

v) Portable

It should be possible to apply the recommended technique easily to any gridded dataset.

2. Definition

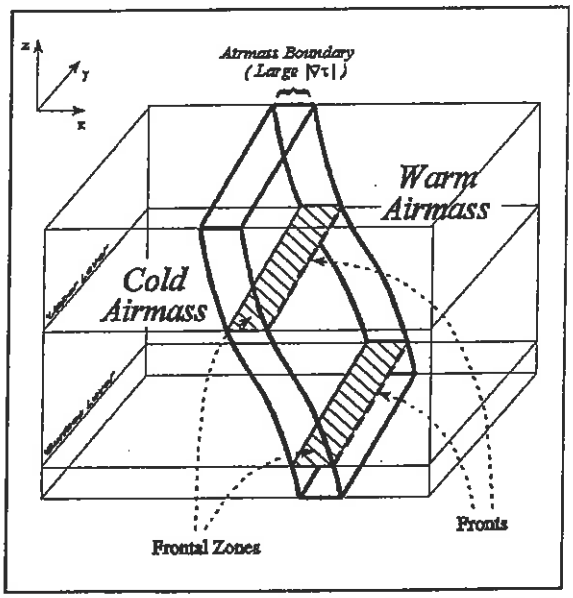

Figure 1: Schematic representation of a frontal surface in 3-dimensions (τ is a thermodynamic variable).

At the most basic, or *primary* level a front can be defined as the 'boundary between airmasses of different thermal characteristics' (see Meteorological Office, 1991). This boundary comprises a thin layer, or non-rigid slab-like region, in three-dimensional space, within which there are, naturally, large horizontal gradients in the thermal characteristics (such a layer is

marked in bold outline on Figure 1). The elongated region in which this layer intersects a pre-defined pseudo-horizontal surface (such as a pressure surface) defines a *frontal zone* on that surface. The warm-air boundary of this frontal zone (ie a line) then defines a *front*. If the pre-defined surface is close to the earth's surface, as on many charts, then any fronts are *surface fronts*. Similarly, if the pre-defined surface represents some level higher up in the troposphere, then the fronts can be referred to as *upper fronts*.

Other 'non-thermal' variables, such as vorticity, can be viewed as *secondary* characteristics, which are not sufficient, by themselves, to define a front. A trough-line on a surface chart, for example, may be characterised by a vorticity strip, a cloud band and a precipitation band but would not, if there were no thermal contrast, be classified a front. Such a distinction seems desirable, and is retained here.

3. Earlier work

The first publication concerned with objective identification of fronts was by Renard and Clarke (1965). Their paper defined a methodology for identifying and locating fronts in gridded datasets, and this methodology has been utilised by many subsequent authors. Table 1, which resulted from a thorough literature search, summarises the main published work in the field and is laid out according to Renard and Clarke's methodology. Row 12 was added to indicate the main technique proposed in this paper. The meaning of the symbols in table 1, and elsewhere in this paper, is given below:

τ	surrogate for any thermodynamic variable
μ	surrogate for any vector
Ψ	surrogate for any scalar variable
(s,n)	rotated Cartesian co-ordinates (appendix 1)
$\mu_x, \mu_y, \mu_s, \mu_n$	components of μ
$\pm\mu$	surrogate for any 'axis' (appendix 2)
∇	2-D horizontal/pressure level gradient operator
θ	potential temperature
θ_w	wet-bulb potential temperature
θ_e	equivalent potential temperature
$\overline{\theta}$	layer mean potential temperature
T	temperature
$\overline{T}$	layer mean temperature
V	total horizontal wind velocity
V_G	horizontal geostrophic wind velocity
V_{front}	speed of movement of a front in a perpendicular direction
ω_{fr}	component of vertical velocity attributable to surface friction
ω_{QG}	component of vertical velocity attributable to quasi-geostrophic forcing
A_Ψ	total advection of scalar variable Ψ
$A_{G\Psi}$	geostrophic advection of scalar variable Ψ
P	pressure
P_{MSL}	mean sea level pressure
RH	relative humidity
K_n	masking criteria threshold value (n=integer)
$_{ABZ}$	subscript denoting 'adjacent baroclinic zone'
Z_T	thickness
Z_T^*	equivalent thickness $\left(=-\frac{g}{R}\sum_{lev1}^{lev2}\overline{T}_e \ln\left(\frac{P_u}{P_l}\right)\right.$ with
g	acceleration due to gravity
R	universal gas constant
$\overline{T}_e$	layer mean equivalent temperature
P_u	pressure at top of layer
P_l	pressure at bottom of layer)

Renard and Clarke's methodology involved selecting *one* variable (column B in table 1), on *one* particular, pseudo-horizontal atmospheric level (column A (model gridlength also shown)), deriving a diagnostic quantity based on this variable (C), which should relate directly to the location of any fronts, recommending a technique for plotting fronts using this diagnostic (D), and then subsequently applying miscellaneous secondary criteria to *mask out* regions where fronts identified using the initial diagnostic were considered to be spurious (E). Column F relates to the accuracy of each method. It was prepared by intercomparing the extent to which these methods replicated manual frontal analyses, and is based on examples presented within each paper and on any comments and statistics provided by the respective authors. The geographical and temporal scope of the data each had used is given in column G. As fronts are likely to be more difficult to identify over elevated orography than over oceans, the accuracy quoted in column F will depend, in part, on the verifying domain shown in column G.

Renard and Clarke (1965) identified the 'thermal front parameter' (*TFP*) (row 1, column C in table 1) as being an important diagnostic for locating fronts. *TFP* is a scalar variable, representing the magnitude of the following: 'the gradient of the magnitude of the gradient of a thermodynamic scalar quantity, resolved into the direction of the gradient of that quantity'. The thinking behind this definition was that maxima, or ridge lines in the field of *TFP*, would coincide with the warm air boundary of any frontal zones, and thus, in accordance with the definition in section 1, would be co-located with fronts. This

·Publication	(A) Level [Grid-length]	(B) Var. (τ=)	(C) Diagnostic (2-dimensional horizontal operators)	(D) Method	(E) Criteria to be met ('masking')	(F) Relative Accuracy (see text)	(G) No. of Exa-mples
1) Renard and Clarke (1965)	850mb, Terrain [381km]	θ	$TFP(\tau)$= $-\nabla\lvert\nabla\tau\rvert\cdot\frac{\nabla\tau}{\lvert\nabla\tau\rvert}$	Manual trace of maxima (ridges)	*Small* regions of +ve TFP ignored	Fair	2x N. Hem.
2) Kirk (1965)	850mb [500km]	θ	$\nabla^2\tau$	Manual trace of minima (troughs)	Nil	Good	1x N. Ameri-ca
3) Clarke and Renard (1966)	850mb [381km]	T	$\nabla\tau\cdot\frac{\nabla(TFP(\tau))}{\lvert\nabla(TFP(\tau))\rvert}$	Contour of zero	$TFP \geq \alpha$ ($\alpha \geq 0$)	Fair/Poor	1x N. Hem.
4) Clarke and Renard (1966)	850mb, 1000mb [381km]	θ	$TFP(\tau)$	Manual trace of maxima (ridges)	i) *Small* regions of +ve *TFP* ignored ii) $TFP >$ 0.15 °C/(100km)^2	Good	6x 1/2 N. Hem.
5) Clarke and Renard (1966)	1000-700mb [381km]	$\overline{\theta}$	$-\nabla^2\tau$= $-TFP(\tau)$ $-\lvert\nabla\tau\rvert\nabla\cdot\frac{\nabla\tau}{\lvert\nabla\tau\rvert}$	Manual trace of maxima (ridges)	Various	Poor	1x 1/2 N. Hem.
6) Huber-Pock and Kress (1981)	850-500mb [not given]	Z_T^*	$TFL(\tau)$= $\nabla(TFP(\tau))\cdot\frac{\nabla(\tau)}{\lvert\nabla\tau\rvert}$	Block out gridboxes which encompass a zero contour	i) $\nabla(TFL(\tau))\cdot\frac{\nabla\tau}{\lvert\nabla\tau\rvert}<0$ ii) $\lvert$along front $\nabla\tau\rvert$ $<\lvert$across front $\nabla\tau\rvert$	Good	1x Europe
7) Cahir and Lottes (1982)	Terrain [~60km]	θ_W	$\lvert\nabla\lvert\nabla\tau\rvert\rvert$	Block out gridboxes where max. in x or y	i) $\nabla^2\tau < 0$ ii) $\nabla^2 P_{MSL} > 0$	Poor (manual analysis suspect)	1x eastern /central U.S.A.
8) Zwatz-Meise and Mahringer (1987)	850-500mb [not given]	$\overline{T}$	$TFP(\tau)$	Manual trace of maxima (ridges)	Cloud band on IR imagery	Fair/Good	3x W. Europe
9) Japan Met. Agency (1988)	1000-500mb [~320km]	Z_T	$TFP(\tau)$	Automatic trace of maxima (ridges)	Nil	Fair/Good	1x Asia + W. Pacific
10) Huber-Pock and Kress (1989)	850-500mb [381km]	Z_T^*	$TFP(\tau)$	Manual trace of maxima (ridges)	$TFP > 2.5$ °K / d^2 (d = 1 grid length)	Good	3x Europe / N. Atlantic
11) Stein-acker (1992)	850mb [not given]	θ_e	$\frac{\partial^2\tau}{\partial s^2}$ [$s \equiv s_1$ where $\lvert\partial^2\tau/\partial s_1^2\rvert$ maximised]	Manual trace of minima, following axes of n	Nil	Fair/Good	1x Europe / NE. Atlantic
12) Hewson (1996)	900mb and 600mb [100km]	θ_W	$\partial(\nabla\lvert\nabla\tau\rvert)_s/\partial s$ [where $s \equiv \pm\nabla\lvert\nabla\tau\rvert/\lvert\nabla\lvert\nabla\tau\rvert\rvert$]	Contour of zero	i) $TFP > K_1$ where $K_1 \sim .35$°C/(100km)^2 ii) $\lvert\nabla\tau\rvert_{(ABC)} > K_2$ where $K_2 \sim 1.2$°C/100km		

Table 1: A summary of methodologies employed in studies concerned with the objective identification of fronts. Also see text.

diagnostic was adopted by many subsequent authors (see column C).

In response to Renard and Clarke, Kirk (1965) (row 2) proposed using the ∇^2 operator as an alternative to the *TFP*. Clarke and Renard (1966) attempted using this (row 5), but achieved little agreement with a manual analysis; indeed the front positions so derived were arguably the worst of any in table 1. It is perhaps because of this that subsequent authors generally restricted themselves to using *TFP*.

In retrospect there was probably one key reason why Clarke and Renard's fronts based on $\nabla^2\tau$ (row 5) were inaccurately positioned. Rather than using a straightforward five-gridpoint finite difference approximation to ∇^2, covering two mesh lengths, they summed two separate terms (row 5, column C). This would have necessitated using basic values from 13 gridpoints, ie covering 4 gridlengths, to derive each value of the diagnostic. With the 381km mesh length available to them, this corresponds to a spread of data of order 1500km, a distance probably too large to enable many atmospheric fronts to be detected. In addition, a (five-point) finite difference approximation to ∇^2 is much more robust, computationally, than are similar approximations to the two separate terms. This is because each of the two terms is based on the quantity $\nabla(\tau)/|\nabla(\tau)|$, ie a unit vector pointing in the direction of the gradient. This quantity is ill-defined wherever $|\nabla(\tau)|$ is small (because a small local change to τ can then have a large effect on the unit vector's direction) and wherever $\nabla(\tau)$ changes direction abruptly. This would not be such a problem were it not for the fact that such regions regularly occur close to frontal zones. The thermal ridge (or 'warm conveyor belt') found immediately ahead of some cold fronts is a prime example of such a region: here $|\nabla(\tau)|$ is small and $\nabla(\tau)$ changes direction abruptly. Thus it seems plausible that if Clarke and Renard had not split up $\nabla^2\tau$ into two components, better agreement with the manual frontal analysis would have been achieved, and the direction of subsequent work may have altered somewhat.

Note that one of the two terms which are not computationally robust in the vicinity of fronts is in fact the thermal front parameter. Steinacker (1992) recognised this, and proposed a solution which involved identifying the frontal orientation at each gridpoint, as the solution to an Eigenvalue problem (see row 11 column C: $\pm\hat{s}$ is a *cross-front* unit vector). Cleaner and simpler alternative approaches to the problem, which are based around using the ∇^2 operator, are discussed in section 5.

As well as satisfying the aims listed in section 2 above, any 'optimal' technique for plotting fronts should be wholly automatic (column D). If not it will be time-consuming and, quite clearly, not completely objective. In table 1 there are, somewhat surprisingly, only four past examples where the front plotting is automatic - in rows 3, 6, 7 and 9. Clarke and Renard (1966), in row 3, used a diagnostic prone to computational problems, as they themselves recognised, and as a result achieved unsatisfactory agreement with hand-drawn analyses. The method of Huber-Pock and Cress (1981), in row 6, achieved greater accuracy, albeit on a very limited area. However, further investigations to be presented in section 5 show that their diagnostic tends to produce broken fronts, and in addition masking criterion (i) is difficult to interpret physically. Cahir and Lottes (1982), in row 7, used a similar 'gridbox-searching' technique (column D). They succeeded in highlighting zones about 100km wide which contained fronts, but failed to plot lines to actually represent them. The Japan Meteorological Agency (1988), row 9, appear to have been most successful, although their technique does require non-trivial algorithms to automatically trace maxima (column D), and includes no way of tuning according to frontal intensity (column E).

Out of the methodologies listed in table 1 only one appears to have been used in preference to subjective frontal positioning in published research, that is the method of Huber-Pock and Kress (1989) (row 9). The applications of this method have been quite wide-ranging: Hoinka and Volkert (1992) and Heimann (1992) used the technique to locate fronts over the Alps, Sabo (1992) looked at the *TFP* around cut-off lows, Zwatz-Meise and Bendl (1992) investigated links between precipitation, imagery and positive vorticity advection, Zwatz-Meise and Hufnagl (1990) studied ana- and kata-fronts using imagery and the *TFP*, and Zwatz-Meise and Mahringer (1990) examined interactions between jet-streaks and frontal zones. The technique is also used operationally by forecasters in Austria. It should be emphasised however that in all these cases the fronts had to be drawn manually, on the basis of the field of *TFP*.

4. Graphical considerations

A key facet of the work presented in this paper is the coupling together of mathematical and graphical techniques. The graphical techniques to be described here are thus closely

INSERT - FIG 2

allied to the Renard and Clarke front-plotting packages. The first stage (left hand panels)

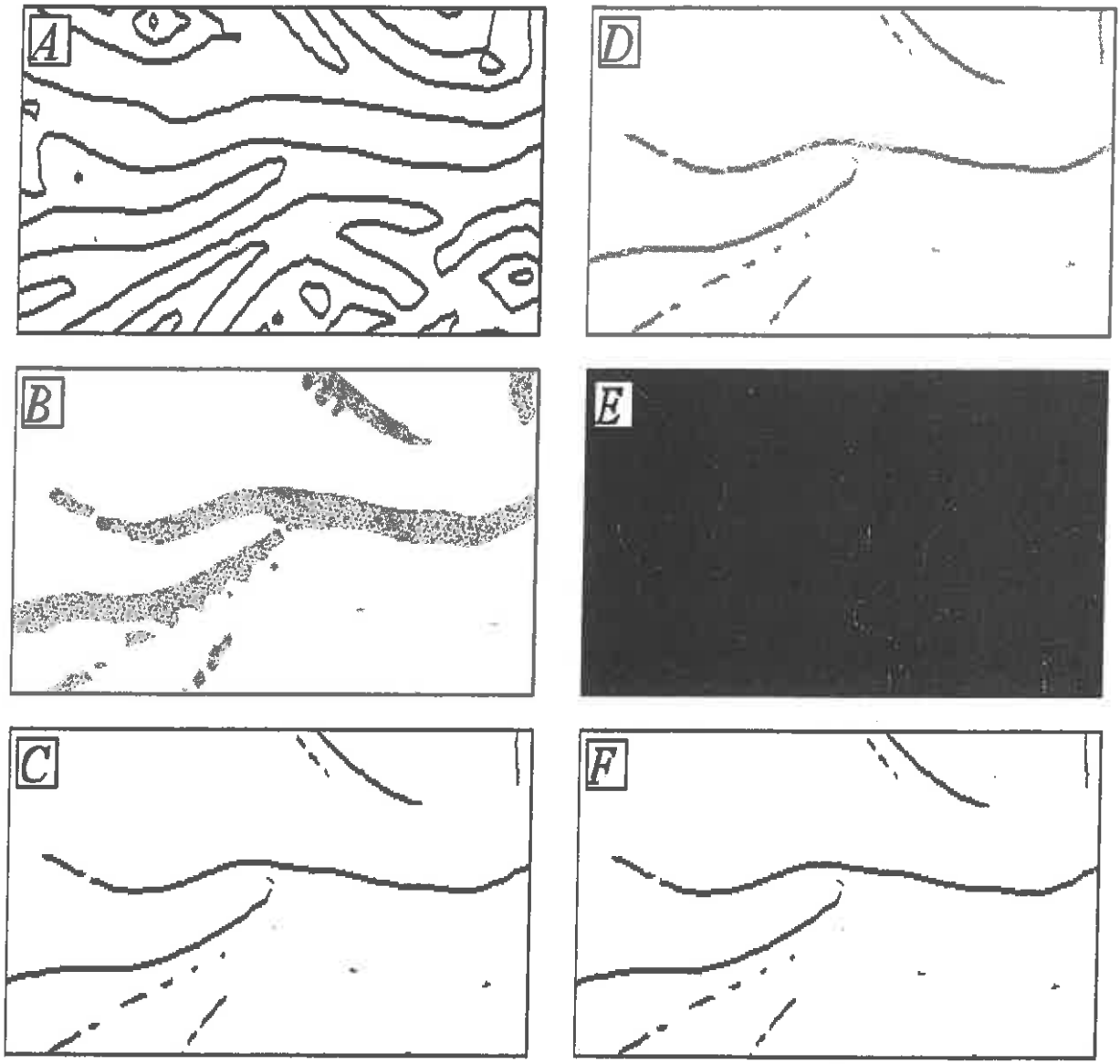

Figure 2: Sequence illustrating the graphical steps required to display linear features (*f*), such as atmospheric fronts, as coloured line segments. At least 3 variable fields are required (introduced at stages A, B and E).
Grey shading (visible on panels B and D) represents 'transparent'.
A is a contour plot of the variable which identifies *f* (zero contour only). B is a colour-fill plot (in white and 'transparent') of a masking variable for *f*. C is the result of overlaying B on A. D results from a colour operation 'convert black to transparent' effected on C. E is a colour-fill plot in two (or more) colours of a colouring variable for *f*. F is the result of overlaying D on E. See text for further explanation.

methodology described in section 3.

As a graphical entity, fronts can be described as 'lines of finite length' (note that other meteorological features, such as jet streams, fall into the same category). Figure 2 illustrates how 'lines of finite length' can be generated using contouring and colour-filling techniques common to standard graphics produces black line segments, whilst a second, optional stage (right hand panels) converts to coloured line segments. One natural use of coloured line segments would be for showing warm and cold fronts in red and blue respectively.

Note that grey on figure 2 is used to denote 'transparent'.

4.1 Black line segments

The steps required to produce the basic line segment plot (panel C) are simply these (letters refer to panel labels):

1) plot A (contour in black)
2) plot B ('colour-fill' in white/transparent)
3) overlay B on A. giving C

This requires at least 2 variable fields:

- One *locating* variable (panel A)
- One or more *masking* variable(s) (B)

If, say, there were two masking variables (call B1 and B2), then step 3 above would be 'overlay B1 and B2 on A, giving C'.

Note that the 'locating variable' above equates to the 'diagnostic' on table 1 (column C), whilst the 'masking variables' equate to the 'criteria to be met' (column E). However, only if a *specific value* of a given diagnostic, as opposed to a maximum or a minimum, coincided with a front would it be possible to apply the graphical steps described above (ie only for rows 3, 6 and 12 on table 1).

4.2 Coloured line segments

Panels D, E and F depict the additional steps required to convert black line segments into coloured line segments. Following on from steps 1 to 3 above these are:

4) transpose colour on C, giving D
5) plot E (colour-fill)
6) overlay D on E, giving F

Thus converting panel C to panel F requires, additionally:

- One *colouring* variable (panel E)

Any number or range of colours may be used at stage 5 (panel E). Uses of coloured line segments will be discussed in section 6.

4.3 Mathematical description

A 'mathematical description' of the line segments shown in panel C of Figure 2 comprises one locating equation which must be satisfied, and n masking inequalities which must be satisfied, where 'n' is the number of masking variables:

- (locating variable) = 0
- (masking variable 1) > K_1

:

- (masking variable i) > K_i

:

- (masking variable n) > K_n

($n \geq 1$ and $K_i \geq K_{i(min)}$ for all i)

K_i is a masking criterion threshold value, corresponding to the boundary between the two 'colours' on panel B. The grey region - that is to say the region which is left 'transparent' - corresponds to where the inequality is satisfied, whilst white is plotted where it is not satisfied. The K_i values could be adjusted, to apply more or less stringent masking. Less stringent masking would naturally decrease the size of the white (masking) region, and thus increase the total length of line segments (shown on panel C).

For many entities there will be a lower bound on adjustments which can be made to the K_i values. This lower bound will exist to prevent the initial definition of the entity in question being violated. For example, a locating equation for a jet stream might also be satisfied along *minima* in a wind speed field; it would be imperative that some masking be applied in order to remove at least these minima. The set of values which correspond to the lower bounds on adjustments to K_i are given by constants $K_{i(min)} = (K_{1(min)}, \ldots K_{n(min)})$.

When there is considered to be no appropriate lower bound on the value (K_i) of a particular masking variable, then $K_{i(min)}$ is assigned a dummy value which is less than the range of all possible values of the diagnostic in question. This ensures that any 'masking' applied with $K_i = K_{i(min)}$ then has no effect. If the variable were a normal scalar variable the dummy value would be $K_{i(min)}=-\infty$, whilst if the variable were a 'magnitude' the dummy value would be $K_{i(min)}=0$.

4.4 'Absolute' fronts

Clearly the set of line segments remaining if masking has been applied using all thresholds $K_i = K_{i(min)}$ constitutes a special case. It is suggested that the word 'absolute' be used to describe this special case. This introduces terms such as 'absolute fronts' and 'absolute jet streams'.

5. New diagnostics

The front definition given in section 2 can be broken down into fundamental elements which will allow fronts to be represented using the graphical methodology detailed in section 4. These elements comprise a locating variable **[L]**, and 2 masking variables, **[M1]** and **[M2]**, and are described as follows:

[L] A front is a line, adjacent to a baroclinic zone, across which the magnitude of the thermal gradient is changing most abruptly

[M1] The rate of change of thermal gradient across a front, in the direction of the cold air, must be greater than some pre-defined critical value (K_1).

[M2] The thermal gradient in the baroclinic zone adjacent to a front must also be greater than a pre-defined critical value (K_2).

K_1 and K_2 are the masking criteria threshold values. They clearly allow for 'tuning', in accordance with the requirement in section 1(iv) above. They also allow for the definition of an 'absolute front' (section 4.4), wherein $K_{1(min)} = 0$ and $K_{2(min)} = 0$. Setting $K_1 = 0$ would allow masking criteria 1 to eliminate *only* the cold air sides of baroclinic zones whilst setting $K_2 = 0$ would ensure masking criteria 2 had no effect (ie '0' is a dummy value).

Note that the breakdown just described also corresponds with how a forecaster is likely to recognise a front in a numerical model thermal field.

It will now be instructive to consider three types of front, of increasing levels of complexity:

Type 1 front: a straight front with no thermal gradient in the along-front direction

Type 2 front: a straight front with a non-zero thermal gradient in the along-front direction

Type 3 front: a curved front which may or may not have a thermal gradient in the along-front direction

Type 3 is the general case; types 1 and 2 are special subsets of this. For each of these 3 categories we will define locating and masking variables (in sections 5.1, 5.2 and 5.3). Then we will present examples of objective fronts identified using some of the recommended diagnostics on gridded data from an operational numerical model (section 5.4). In section 5.5 we define a standard colouring variable, for discriminating between warm and cold fronts, and then in 5.6 and 5.7 discuss the use of different atmospheric levels and different thermal parameters. Choice of appropriate values for K_1 and K_2 is dealt with in 5.8.

5.1 A type 1 front

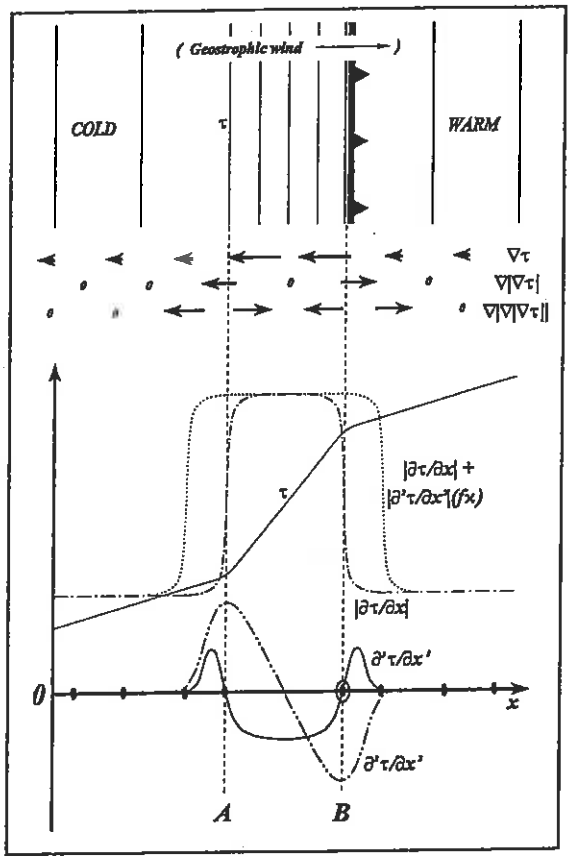

Figure 3: *Top* shows idealised plan view of contours of a thermodynamic variable τ in the vicinity of a straight (cold) front with no along-front thermal gradient (ie a type 1 front). Lines A and B delineate the frontal zone. *Arrows* represent various vector differentials of τ. *Graphs* show schematically how τ and various scalar differentials of τ vary in the cross-front (x) direction. Points marked on the x-axis show where $\partial^3\tau/\partial x^3 = 0$; those intersected by lines A and B are precise, others are schematic. The ringed dot coincides with the front. fx represents a fractional number (f) of gridlengths (x).

Figure 3 depicts a type 1 (cold) front. It shows an idealised plan view of the distribution of some thermal field τ in the vicinity of the front (top), as well as schematic examples of horizontal vector and scalar differentials derived from this field (below). Because there is no variation in τ in the y direction, all 2-dimensional

horizontal gradient operators are equivalent to their one-dimensional x-direction counterparts. For example, $\nabla\tau = -i\partial\tau/\partial x$. It also follows, here, that $\partial^2\tau/\partial x^2 = \nabla^2\tau = -TFP(\tau)$.

The region bounded by vertical dashed lines A and B is the frontal zone; line B coincides with the front. The question is how best to mathematically locate the position of B. As the curve representing $\partial^2\tau/\partial x^2$ (=-*TFP*) reaches a minimum at the front, a line which coincided with this minimum could naturally be used as a front locator (as in rows 1,2,4,5,8,9 and 10 on table 1). This line could be drawn as a contour through locations where the gradient of $\partial^2\tau/\partial x^2$ equals zero, ie:

$$\partial^3\tau/\partial x^3 = 0 \qquad \cdot(1)$$

This is thus the locating equation **[L]** for the type 1 front. The function $\partial^3\tau/\partial x^3$ is sketched on Figure 3 (solid line). Dots on the x-axis show schematically where (1) is satisfied; however only the ringed dot represents a front. Thus a method is needed to mask out those dots which are not ringed. For a type 1 front masking criterion **[M1]** is represented, as an inequality, as follows:

$$\partial^2\tau/\partial x^2 < K_1$$

$$\text{ie} \quad (-\partial^2\tau/\partial x^2) > K_1 \qquad \cdot(2)$$

$$\text{where} \quad K_{1(min)} = 0$$

Note that it is where the inequality is satisfied that the front is retained (in accordance with the convention adopted in section 4).

The representation of criterion **[M2]** is less straightforward. It could conceivably involve complex algorithms for searching, from each gridpoint, through a field of $\partial\tau/\partial x$, to find a representative value for 'the adjacent baroclinic zone'. A simpler alternative is to utilise Taylor's series, for estimating the value of a function ϕ at a location $(x+\delta x)$, ie

$$\phi(x+\delta x) = \phi(x) + (\delta x)\,\phi'(x) + (\delta x^2/2!)\,\phi''(x) + \ldots$$

Replacing ϕ by $\partial\tau/\partial x$, ignoring second and higher order terms, and working with gradient magnitudes only gives:

$$|\partial\tau/\partial x|_{(\sim ABZ)} = |\partial\tau/\partial x|_{(x)} + (f\mathcal{X})\,|\partial^2\tau/\partial x^2|_{(x)} \qquad \cdot(3)$$

where *'~ABZ'* stands for 'estimated value in the adjacent baroclinic zone', and represents a location $x+f\mathcal{X}$, where $f\mathcal{X}$ is a fractional number (f) of gridlengths ($\mathcal{X}$) in the direction in which the gradient is increasing most rapidly. Provided f is small enough for $|\partial^2\tau/\partial x^2|_{(x)}$ to still apply (say ~0.5) then (3) should provide reliable estimates. The general form of the function produced by (3) is shown on Figure 3 (dotted line). Criterion **[M2]** now becomes:

$$|\partial\tau/\partial x|_{(\sim ABZ)} > K_2$$

$$\text{where} \quad K_{2(min)} = 0 \qquad \cdot(4)$$

We now have one equation (1) and two inequalities ((2) and (4)) which together constitute the mathematical description of a type 1 front (as proposed in section 4.3).

To provide a full mathematical description of either a type 2 front or a type 3 front appropriate counterparts need to be found for (1), (2) and (4).

5.2 A type 2 front

For brevity just the front locator **[L]** will be considered for a type 2 front (ie just the counterpart to (1)).

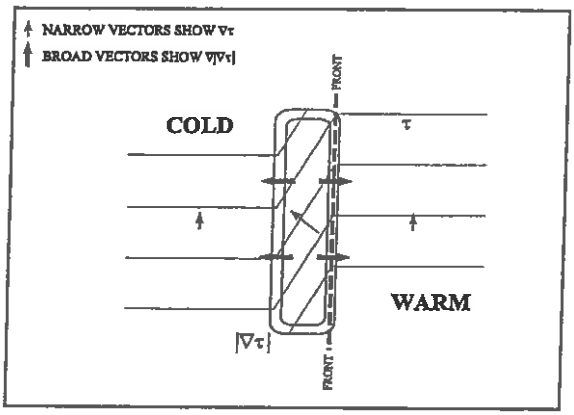

Figure 4: Schematic plan-view of a straight front with an along front thermal gradient (ie a type 2 front). Thin contours show a thermal field τ, thick closed contours the field $|\nabla\tau|$, and vectors are as described in the key.

Figure 4 depicts an idealised type 2 front. The main difference in the diagnostics compared to type 1 is that $\nabla\tau$ is not unidirectional. This vector will always change direction along a type 2 front. For this reason the *TFP*, which represents changes in $\nabla|\nabla\tau|$ in the direction of $\nabla\tau$, is not uniquely defined along the front. This will generate some noise in computed fields of *TFP*. In practice the noise level generated may not be too serious a problem - the extent to which the *TFP* has been utilised in past work (section 3) is perhaps evidence of this. However if further

derivatives are computed from this field, as required in order to generate an automatic front locator, ie a *TFP* counterpart to (1), then the noise level may become unacceptable. Note that two of the three automatic front-plotting techniques in table 1, ie in rows 3 and 6, utilised further derivatives of *TFP* in this way. Clarke and Renard acknowledged that their method (row 3) was inaccurate. The thermal front locator or *TFL* of Huber-Pock and Kress (row 6) will also be shown to have noisy characteristics.

Unlike $\nabla\tau$, the vector field of $\nabla|\nabla\tau|$ is essentially unidirectional in the vicinity of a type 2 front (figure 4), and thus computationally more robust in the area of interest. This vector field will generally be divergent within the frontal zone, and convergent immediately outside. The front is thus the line of zero divergence of $\nabla|\nabla\tau|$, ie:

$$\nabla\cdot\nabla|\nabla\tau| = 0 \quad \text{or} \quad \nabla^2|\nabla\tau| = 0 \qquad \cdot(5)$$

5.3 A type 3 front

Synoptic charts and numerical model thermal fields indicate that most atmospheric fronts are curved and possess a finite along-front thermal gradient. As such they belong uniquely to this type 3 category. Figure 5 depicts the field of $|\nabla\tau|$ around one such front.

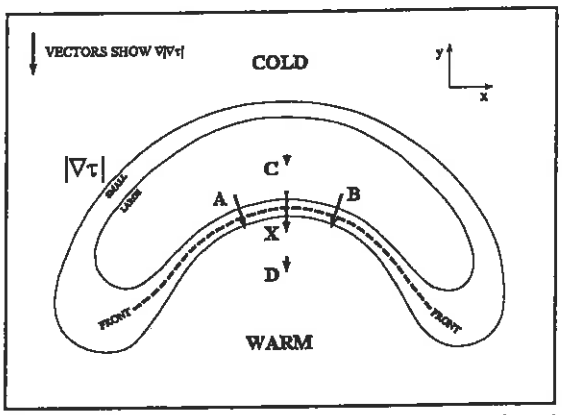

·Figure 5: Schematic showing contours of $|\nabla\tau|$ and selected vectors of $\nabla|\nabla\tau|$ in the vicinity of a curved front (ie a type 3 front). Letters are referenced in the text.

Consider the regular 5-point array of vectors of $\nabla|\nabla\tau|$ labelled A, B, C, D and X.These points might correspond to numerical model gridpoints. Assume that the vectors at D, C and X are unidirectional, and that those at C and D are of equal magnitude. If (5) could be used to correctly locate the front in this final case, then computing the divergence of $\nabla|\nabla\tau|$ at point X, as in (5), using simple first order finite differencing, should give a value zero. This will not be the case because the vectors at A and B are convergent, on account of the curvature of the front. Thus the errors involved in using (5) to locate type 3 fronts will depend on the true frontal curvature. These errors will be such that magnitude of the frontal curvature is exaggerated.

The solution to problems associated with curved fronts is to compute the 'along-vector divergence', which has also been referred to (Saucier, 1955, page 323) as the *stretching* part of the total divergence. This terminology is not in common use; its meaning is laid out in Appendix 1. For a type 3 front (5) can thus be rewritten:

$$\partial(\nabla|\nabla\tau|)_{\hat{s}}/\partial s = 0 \qquad \cdot(6)$$

where unit axis $\hat{s} = \pm\nabla|\nabla\tau|/|\nabla|\nabla\tau||$

A 'unit axis' is essentially the same as a unit vector, except that it possesses an orientation instead of a direction (hence the '±'; see Appendix 1 for further discussion).

The main concern with regard to evaluating (6) numerically is what is the most meaningful way of defining $\hat{s}$? Whatever method is used it should be analogous to drawing a streamline through a vector field (see Figure A1 in Appendix 1), wherein the streamline approximates the cross-front orientation. There are two fundamental approaches: either define $\hat{s}$ to simply be parallel to $\nabla|\nabla\tau|$ at each gridpoint (the 'centre point method'), or allow the values of $\nabla|\nabla\tau|$ at surrounding gridpoints to also have some influence (a 'smoothing method').

Using the centre point method creates problems. Consider, for example, points C and D on Figure 5. At each of these $|\nabla|\nabla\tau||$ is small, and thus $\hat{s}$ is ill-defined. This is analogous to there being erratic or discontinuous cross-front streamlines, and in practice means the zero contour from (6) will also behave erratically. Using a smoothing, or averaging method can overcome this.

It is perhaps most appropriate to perform averaging across arrays of five grid points, as this will be the number of grid points involved each time the $\partial/\partial s$ part of (6) is computed (assuming simple first order finite differencing is used). The simplest approach then is to give each of the five points equal weight. Thus at each gridpoint $\hat{s}$ is evaluated by computing a mean of five values of $\nabla|\nabla\tau|$, treating each such value as an axis (ie $\pm\nabla|\nabla\tau|$) as opposed to a vector. Appendix 2 details how to compute a mean axis (in section (i)), and illustrates how this is fundamentally different to computing a mean

vector (in sections (ii) and (iii)). Deriving a mean vector, whilst rather more straightforward, is incorrect; vectors cancel out across baroclinic zones, causing noise similar to that inherent in using the centre point method to define $\hat{s}$.

So the full numerical procedure for computing $\partial(\nabla|\nabla\tau|)_s/\partial s$ (equation (6)), at each gridpoint, is as follows:

i) Derive a '5-point mean axis' (as in Appendix 2)
ii) Resolve the four outer vectors into the +ve $\hat{s}$ direction
iii) Compute *total* divergence of the *resolved* vectors, using simple first order finite differencing

The divergence calculated in (iii) is then the required quantity.

The method described immediately above is unusual in that the conventional way of evaluating the left hand side of (6) would involve re-writing the equation first, using unit vector dot products to represent derivatives in particular directions, ie:

$$\begin{aligned} &\text{substitute} && \nabla|\nabla\tau| = \mu \\ &\text{then (6)} \rightarrow && \partial\mu_s/\partial s = 0 \\ &\text{but} && \partial\mu_s/\partial s = (\nabla(\mu\cdot\hat{s}))\cdot\hat{s} \\ & && = (\nabla(\mu\cdot\mu/|\mu|))\cdot(\mu/|\mu|) \\ & && = (\nabla|\mu|)\cdot(\mu/|\mu|) \end{aligned}$$

$$\text{thus} \qquad (\nabla|\nabla|\nabla\tau||\cdot\nabla|\nabla\tau|)/|\nabla|\nabla\tau|| = 0 \qquad \cdot(7)$$

A physical interpretation of (7) can be obtained by referring back to the vectors on Figure 3. It should be clear why the dot product of $\nabla|\nabla|\nabla\tau||$ and $\nabla|\nabla\tau|$ will give zero along the boundaries of the frontal zone (ie lines A and B).

Thus we no have two representations, (6) and (7), of the locating equation **[L]** for the general type 3 front. The main published alternative to (6) and (7) is the *TFL*, or thermal front-locator, of Huber-Pock and Kress (table 1, row 6). Re-writing this in full gives:

$$\nabla(-\nabla|\nabla\tau|\cdot(\nabla\tau/|\nabla\tau|))\cdot(\nabla\tau/|\nabla\tau|) = 0 \qquad \cdot(8)$$

Finally in this section inequalities representing masking criteria **[M1]** and **[M2]** will be re-written for the type 3 front.

A quantity representing masking criterion **[M1]** should indicate the cross-front rate of change of thermal gradient *and* distinguish between the warm and cold sides of baroclinic zones. The latter necessarily introduces the unit vector $\nabla\tau$. There are perhaps two natural diagnostics which can represent criterion **[M1]**. First there is the *TFP;* written fully this is:

$$\begin{aligned} &(-\nabla|\nabla\tau|\cdot(\nabla\tau/|\nabla\tau|)) > K_1 \\ &\text{where} \qquad K_{1(min)} = 0 \end{aligned} \qquad \cdot(9)$$

Alternatively, one could write:

$$\begin{aligned} &|\nabla|\nabla\tau||\,(sign[\nabla\tau\cdot\nabla|\nabla\tau|]) > K_1 \\ &\text{where} \qquad K_{1(min)} = 0 \end{aligned} \qquad \cdot(10)$$

The function '*sign*' operates on the contents of the square brackets, returning a value '+1' if the contents is positive, and '-1' if it is negative (ie analogous to the *FORTRAN* function of the same name). As with (6), a smoother, more meaningful field will be represented if some averaging is performed. Averaging values of $[\nabla\tau\cdot\nabla|\nabla\tau|]$ across 5 grid point arrays should prevent localised negative values from occasionally appearing in the middle of tongues of warm air.

To represent criterion **[M2]** for the type 3 front we refer back to equation (3), and re-write for a full 2-dimensional field, ie:

$$|\nabla\tau|_{(-ABZ)} = |\nabla\tau|_{(x,y)} + (f\chi)\,|(\nabla|\nabla\tau|)_s|_{(x,y)}$$

$$\text{where} \quad s = \nabla|\nabla\tau|$$

Then for the type 3 front criterion **[M2]** is simply represented as:

$$\begin{aligned} &|\nabla\tau|_{(-ABZ)} > K_2 \\ &\text{where} \qquad K_{2(min)} = 0 \end{aligned} \qquad \cdot(11)$$

$$\text{and} \qquad |\nabla\tau|_{(-ABZ)} = |\nabla\tau|_{(x,y)} + (f\chi)\,|\nabla|\nabla\tau||_{(x,y)}$$

We set $f = 1/\sqrt{2}$ to correspond, in this two dimensional case, to the distance from a gridpoint to the centre of an adjoining gridbox.

5.4 Examples

In this section the practical value of the various diagnostics proposed for identifying the general type 3 front will be assessed, using data from the operational U.K. Meteorological Office limited area model (LAM). Whilst the LAM is run with a horizontal resolution of about 50km, raw

INSERT - FIG 6

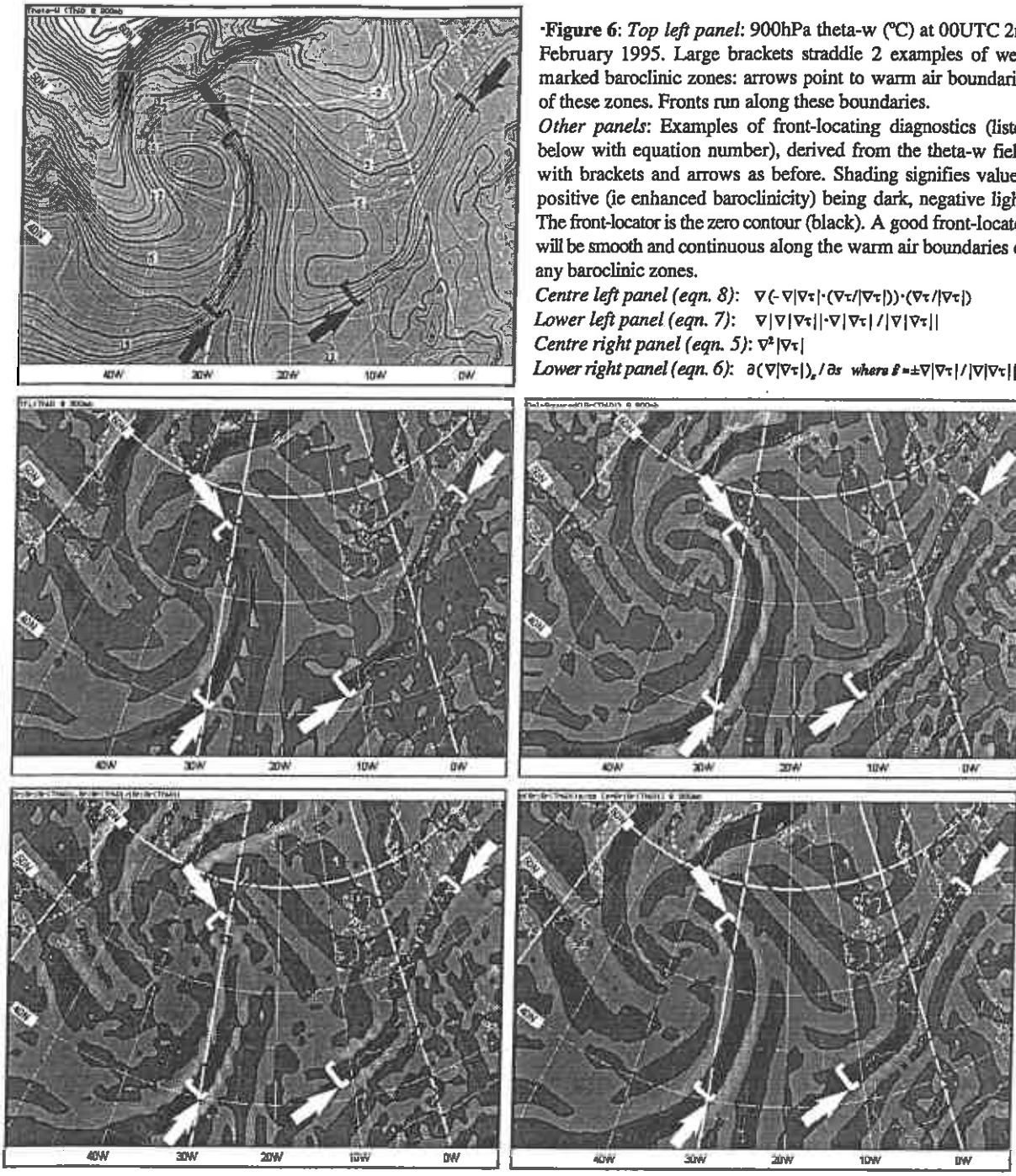

Figure 6: *Top left panel*: 900hPa theta-w (°C) at 00UTC 2nd February 1995. Large brackets straddle 2 examples of well-marked baroclinic zones: arrows point to warm air boundaries of these zones. Fronts run along these boundaries.
Other panels: Examples of front-locating diagnostics (listed below with equation number), derived from the theta-w field, with brackets and arrows as before. Shading signifies values; positive (ie enhanced baroclinicity) being dark, negative light. The front-locator is the zero contour (black). A good front-locator will be smooth and continuous along the warm air boundaries of any baroclinic zones.
Centre left panel (eqn. 8): $\nabla(-\nabla|\nabla\tau|\cdot(\nabla\tau/|\nabla\tau|))\cdot(\nabla\tau/|\nabla\tau|)$
Lower left panel (eqn. 7): $\nabla|\nabla|\nabla\tau||\cdot\nabla|\nabla\tau|/|\nabla|\nabla\tau||$
Centre right panel (eqn. 5): $\nabla^2|\nabla\tau|$
Lower right panel (eqn. 6): $\partial(\nabla|\nabla\tau|)_s/\partial s$ *where* $s=\pm\nabla|\nabla\tau|/|\nabla|\nabla\tau||$

data available for this assessment had been interpolated onto a polar stereographic grid with a resolution of about 100km. The diagnostics have been computed at the 100km resolution, generally using simple first order finite differencing, on a non-staggered grid.

Figure 6 shows a raw 900hPa thermal field (top panel), and 4 front locating diagnostics [L] derived from it. The diagnostics come from equations (5), (6), (7) and (8); the steps used to compute the diagnostic for (6) are those labelled (i) to (iii) in section 5.3. To be useful as front locators the zero contours of the diagnostic fields (shown in black) need to be smooth and continuous along the warm air boundaries of any baroclinic zones. Two such boundaries are highlighted with large arrows (see caption). The following conclusions can be drawn:

- The *TFL* (equation (8), centre left panel) is very fragmented along the two fronts. This is mainly on account of the noise associated with $\nabla\tau$ being poorly defined in the adjacent warm conveyor belt regions.

- Equation (7) (lower left panel) produces a generally continuous but unacceptably noisy frontal structure. The large number of derivatives is probably the cause of the noise.
- Equation (5) (centre right panel) generates clean and reasonably smooth fronts, suggesting it could be used successfully as a front locator. One caveat is that the structure is rather noisy in the southeastern corner of the panel, where elevated topography, such as the Alps, appears to be distorting the thermal pattern. The noise arises mainly because the diagnostic exaggerates frontal curvature.
- Equation (6) (lower right panel) produced the best results. The highlighted fronts are smooth, continuous and correctly located. Structure in the southeastern corner is less noisy than it was for (5), suggesting that fronts reaching this region could be located with reasonable success (problems associated with locating fronts over orography are discussed further in section 5.6).

The characteristics just described are generally replicated on examples from other times (not shown). And whilst different variables could have been used as the thermal parameter τ it is unlikely that the diagnostics' characteristics would have altered greatly as a result (choice of thermal parameter is covered in section 5.7). Thus out of the 4 options considered equation (6) offers the best prospects for use as an objective front locator.

The accuracy with which equation (6) locates fronts relative to where a forecaster would position them on the basis of the thermal field is generally high. Note how the black contours on the lower right panel are very closely aligned with the tips of the white arrows (whose positions were derived subjectively using data on the top left panel). On this and other examples (not shown) the error is usually less than one fifth of a grid spacing and almost always less than one half (=20km and 50km respectively).

Attempts were made to improve on the representation by (6). Although using a reduced size staggered grid to evaluate $\nabla|\nabla\tau|$ should in principle have increased the accuracy of the front positions, it also seemed to result in a slight deterioration in coherence of the diagnostic (as had using the 'centre point method' (section 5.3) to define $\mathcal{F}$). This is undesirable.

We next illustrate the behaviour of the proposed masking diagnostics, using the same case as in Figure 6. On Figure 7 the colour-fill field in the top left panel shows the magnitude of the gradient of τ. The remaining colour-fill fields correspond to masking criteria **[M1]** as represented by (9) (top right panel) and (10) (lower right panel), and masking criteria **[M2]** as represented by (11) (lower left panel). The red lines on each panel are contours of τ at 2°C intervals.

The fact that the colours on each of the two right hand panels match up well indicates that the two ways of representing criteria **[M1]** have the same general characteristics. However there are some differences. In the centre of region 'A', for example, the *TFP* is only weakly positive (yellow shading), whereas the *cross-front gradient change* is strongly positive (orange). This illustrates a disadvantage of using the *TFP*: it will underestimate the cross-front change in gradient when there is a non-zero temperature gradient in the along-front direction. However the *TFP* condition does have the advantage of being able to eliminate spurious fronts which appear across regions where contours of τ are splaying out, such as in region 'B'. This is because in such regions $\nabla\tau$ will be approximately perpendicular to $\nabla|\nabla\tau|$. The *cross-front gradient change* parameter will tend not to do this (note how it is more strongly positive in region 'B'). Thus neither (9) nor (10) then seem to be clearly preferable. In subsequent examples we will utilise condition (9).

The diagnostic in (11) representing masking criteria **[M2]** has the desired effect of 'spreading out' the thermal gradient field (compare the two left hand panels, and refer back to two of the curves on Figure 3 (dotted and dash-dot)). The diagnostic in (11) is also exaggerating the gradient in the centre of baroclinic zones (note the colour changes between the two left hand panels). This was not shown on Figure 3. What is important however is not that the temperature gradient *within* baroclinic zones is correctly represented, but that the values found along any potential fronts give a good estimate of the gradient in the adjacent baroclinic zone (ABZ). This seems to have been achieved here. Note that the true gradient along the baroclinic zone in mid-Atlantic is about 3.5°C per 100km (lightest green, top panel, labelled ABZ), and that the value of the diagnostic along the line of the front on the panel below is similar (between about 3 and 4°C per 100km). Recall that the variable 'f' in (11) was set equal to $1/\sqrt{2}$. Alternative values of 0.5 and 1 were also tried; these tended to produce, respectively, underestimates and overestimates of $|\nabla\tau|_{ABZ}$.

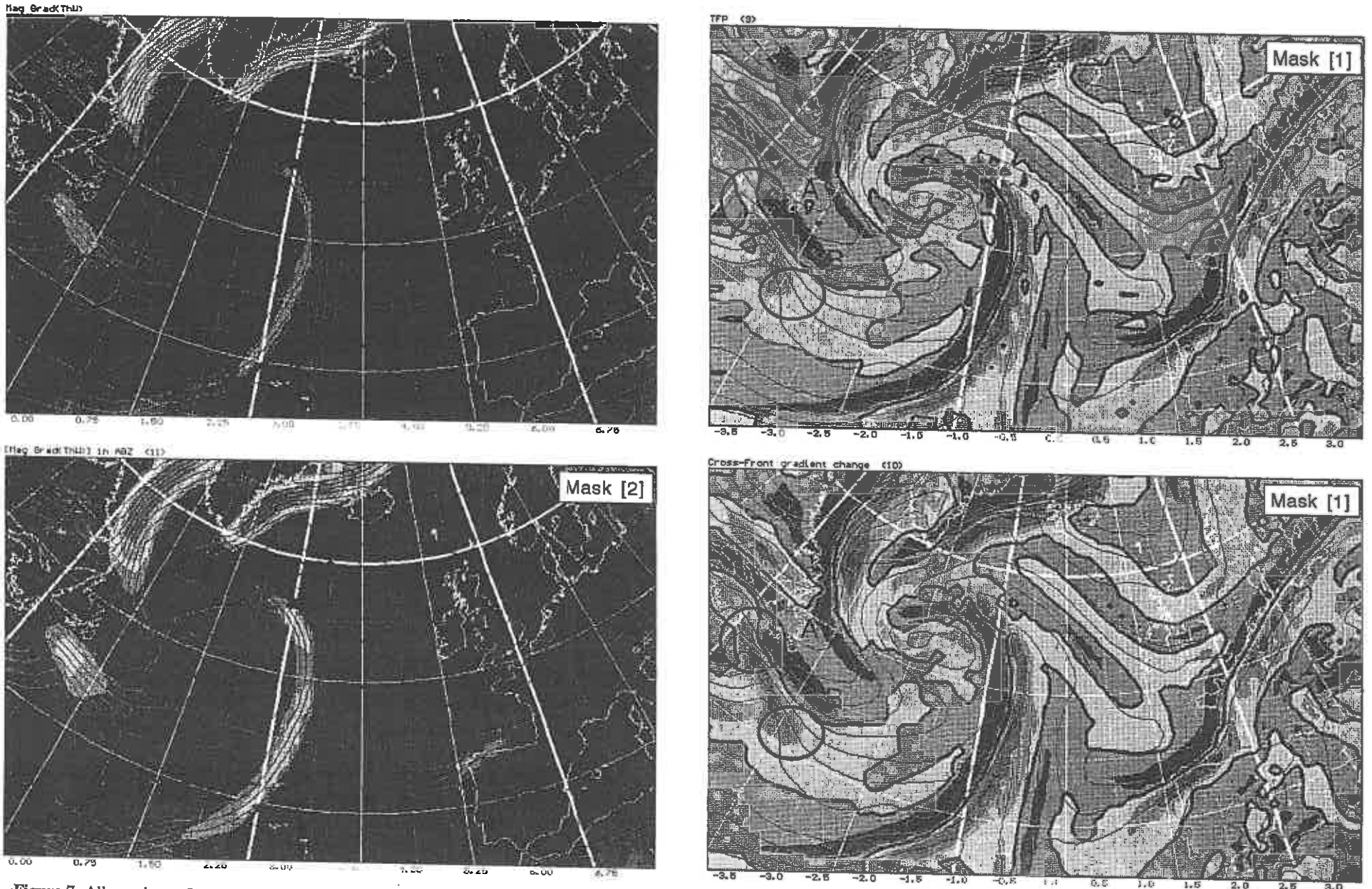

Figure 7: All panels are from a LAM analysis for 00UTC, 2nd February 1995 (same as Figure 6). Red contours show 900hPa θ_w distribution, at 2°C intervals (every panel). Coloured fields are described below (numbers on scales show the lower limit of a colour's range). Labelling highlights features referenced in the text.

Top left panel: $|\nabla\theta_w|$. Scale shows values in °C/100km;
Lower left panel: $|\nabla\theta_w|_{ABZ}$; see equation (11). Scale shows values in °C/100km

Top right panel: TFP= $-\nabla|\nabla\theta_w|\cdot(\nabla\theta_w/|\nabla\theta_w|)$; see equation (9). Scale shows values in °C/(100km)².
Lower right panel: $|\nabla|\nabla\theta_w||(\text{sign}[\nabla\theta_w\cdot\nabla|\nabla\theta_w|])$, see equation (10). Scale shows values in °C/(100km)².

We next demonstrate the impact of *applying* the masking, and changing the masking

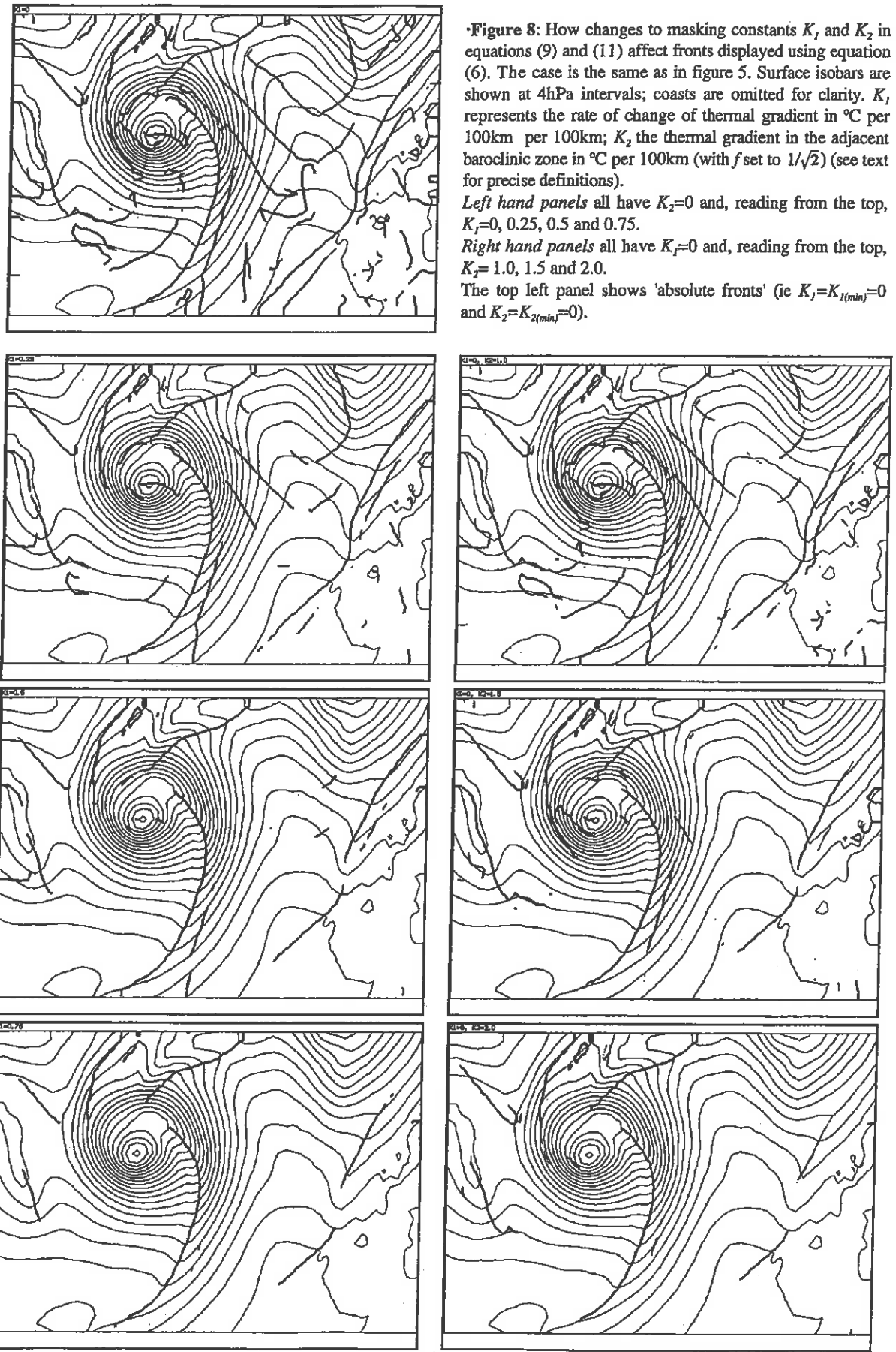

Figure 8: How changes to masking constants K_1 and K_2 in equations (9) and (11) affect fronts displayed using equation (6). The case is the same as in figure 5. Surface isobars are shown at 4hPa intervals; coasts are omitted for clarity. K_1 represents the rate of change of thermal gradient in °C per 100km per 100km; K_2 the thermal gradient in the adjacent baroclinic zone in °C per 100km (with f set to $1/\sqrt{2}$) (see text for precise definitions).

Left hand panels all have K_2=0 and, reading from the top, K_1=0, 0.25, 0.5 and 0.75.

Right hand panels all have K_1=0 and, reading from the top, K_2= 1.0, 1.5 and 2.0.

The top left panel shows 'absolute fronts' (ie $K_1=K_{1(min)}$=0 and $K_2=K_{2(min)}$=0).

constants K_1 and K_2 used in (9) and (11). Figure 8 illustrates this, again using the same case as in Figures 6 and 7.

The top left panel, showing 'absolute' fronts' (section 4.4), is clearly quite noisy. However as the masking constants are increased (ie moving down the figure) the noisy fronts are gradually deleted, leaving what are mainly just smoothly curved fronts on the lower two panels. This implies that (thermally) ·strong fronts are represented better than weak fronts by equation (6), as would be expected. Note also that the fronts retained on the lower two panels are generally co-located with troughs in the isobars. This indicates the following:

- dynamical consistency within the model between thermal fields and wind fields.
- that it is probably not necessary to use vorticity *as well as* thermal fields to locate fronts objectively.
- that the 900hPa level is probably sufficiently close to the earth's surface to represent 'surface fronts'.

5.5 Colouring warm and cold fronts

Fronts can be coloured in different ways to represent different aspects of their structure. For each aspect it is necessary to define one 'colouring variable' (section 4.2), as well as the colours to use and the range of values each of these colours will represent. In this section we describe just a 'standard' colouring method, which will distinguish between warm and cold fronts. Other possibilities are discussed in section 6.

Fronts are generally defined to be cold fronts (blue) or warm fronts (red) according to whether the geostrophic wind implied by the local isobaric pattern is tending to advect them, respectively, towards warmer or colder air. Thus the standard colouring variable for objective fronts is the local geostrophic thermal advection ($A_{G\tau}$), ie

$$A_{G\tau} = V_G \cdot \nabla\tau \qquad (12)$$

where V_G is the geostrophic wind velocity (V is an alternative to V_G). Just two colours are required: red will be used where $A_{G\tau}>0$ and blue where $A_{G\tau}<0$, with boundaries between the two naturally being $A_{G\tau}=0$ (compare with panel E on Figure 2).

The plotting of semicircles and triangles alongside the fronts is essentially a graphical programming task, the description of which is not within the scope of this paper. Neither is the direct plotting of occluded fronts dealt with here (see Steinacker (1992) for further discussion). It should be noted however that the new techniques described in this paper will generally not omit occluded fronts, but instead plot them as either a cold front, or a warm front, or a near-parallel cold front / warm front pair. In some instances these forms of representation could be more informative. Indeed many recent conceptual models of cyclone evolution (Keyser and Shapiro (1990), Monk (1992) and Browning and Roberts (1994)) have not incorporated occluded fronts at all.

5.6 Use of different levels

Column A in table 1 indicates that previous authors have worked with a variety of atmospheric levels. Whilst recognising that the 'layer-integrated' approach utilised by Clarke and Renard (1966, row 5), Huber-Pock and Kress (1981, row 6) and others is probably well suited to identifying fronts which have a significant vertical extent, here a different approach is taken. We use data on individual pressure levels, with a view to separating out fronts near the earth's surface from fronts at other higher levels.

Figure 9 shows one example of objective front positions on 8 atmospheric levels evenly spaced (in pressure) between 1000hPa and 300hPa. The case is the same as that shown in Figures 6, 7 and 8. The fronts were derived using equations (6), (9) and (11), with the same masking constants (K_1,K_2) used at every level (where pressure levels were below the earth's surface τ values were obtained by downward extrapolation). Note that no visual distinction is made between cold and warm fronts; the colour represents pressure level only, according to the scale beneath the figure. Note also that the fronts were 'stacked' on top of one another, working upwards from 1000hPa. Numerous deductions can be made from a close examination of this figure. In particular the advantages of using a multiple-level approach instead of a 'layer-integrated' approach are well illustrated. Specifically the multiple-level approach allows the following features to be immediately recognised (the letters refer to examples seen on Figure 9):

- both deep and shallow frontal systems.
  ['A' is a relatively deep frontal system (1000-500hPa), 'B' a relatively shallow one (1000-900hPa)]

- the slope of frontal surfaces; steeper fronts are liable to be more active. ['C' is a steep frontal surface (1 in 11 from 1000-500hPa) and 'D' a relatively flat one (1 in 120 from 1000-700hPa)]
- regions where upper fronts are beginning to overrun surface fronts - thus denoting 'split fronts' (Browning and Monk (1982)) and warning of possible convective instability. [the cold front at 'E' has a pronounced forward slope. SFERICS reports registered along this front segment in the previous 6 hours indicate there was convective instability]
- elements of the three-dimensional frontal structure around (developing) cyclones. [for example, in area 'F' the warm core enclosed between the pairs of fronts can be seen to be helical in nature (the associated low had just undergone explosive development)]

Whilst output such as that shown on Figure 9 can be very instructive, a more compact format is desirable. It is recommended that just two 'standard' levels be utilised; one to represent 'surface fronts', and the other 'upper fronts'. Many of the above features should remain visible.

In selecting a level to represent 'surface fronts' a compromise has to be met between being sufficiently close to the ground for non-vertical fronts to be located with reasonable accuracy, and being sufficiently far away for the frontal signature to not be dominated by differential surface heat and moisture exchanges, such as are observed near to coasts and marked sea surface temperature gradients. Levels to consider lie approximately in the range 1000 to 800hPa. On Figure 9 many of the 1000hPa fronts are unrelated to surface troughing, and also unrelated to the fronts at higher levels. For example the 1000hPa fronts (black) south of Iceland and Ireland are both symptoms of cold air pools which formed over adjacent land as a result of nocturnal cooling. Such shallow diumal features should probably not be retained as fronts. Thus the 1000hPa level can be considered inappropriate. The 800hPa level (red) is better, but perhaps prone to be too remote from the surface trough line in regions where the frontal slope is relatively small, such as in area 'B'. The leaves 900hPa (dark red) as the level we recommend for representing 'surface fronts' (as used on Figures 6 and 7).

The choice of level to represent 'upper fronts' also requires compromise. The level must be sufficiently remote from the surface front level for there to be added value in plotting upper fronts (at 700hPa fronts were generally considered, on the basis of many examples, to be 'too' similar to those at 900hPa). From a practical perspective however the chosen level should be sufficiently low down for there to be a regular connection with significant weather at the surface, notably precipitation. This probably rules out levels at 500hPa and above; note how many such 'fronts' on Figure 9 (dark green and blue) appear to be unconnected to fronts at lower levels, and also unconnected to isobaric troughing at the surface. The 600hPa level (light green) was selected as the best overall alternative for representing 'upper fronts'.

Forecasters in the U.K. Met. Office frequently consult model fields at the 850hPa level when locating surface fronts. This is very close to the 900hPa level recommended here, and thus consistent with our approach (note however that errors associated with using 850hPa may be slightly larger when the frontal slope is small). Upper fronts are generally not plotted operationally.

The one principal disadvantage of using low-level pressure surfaces is that they intersect orography. This degrades numerical model τ values in mountainous regions in two ways. Firstly, such values are based on a downward extrapolation from other τ values, in which a hypothetical lapse rate has had to be assumed. And secondly they will undergo much larger temporal changes, as a result of daytime insolation, than will τ values on the same pressure surface in low-lying regions nearby. These two factors can lead to spatial discontinuities in τ which are tied to variations in topography (and time of day), and which can manifest themselves as spurious, quasi-stationary, objective fronts (such as the black 1000hPa front around the Alps on Figure 9). It should be possible to overcome such problems, to a large extent, by using terrain-following surfaces instead of pressure surfaces. Such data were not readily available for this study, but certainly warrant future investigation. Note that the region represented in examples in this paper is predominantly oceanic, where there should be little difference between the two approaches.

5.7 Choice of thermal parameter

Whilst the examples presented in sections 5.4 and 5.6 utilised θ_w (wet-bulb potential temperature) as the thermal parameter τ, the primary concern there was the behaviour of the proposed *diagnostics*, and this should be largely

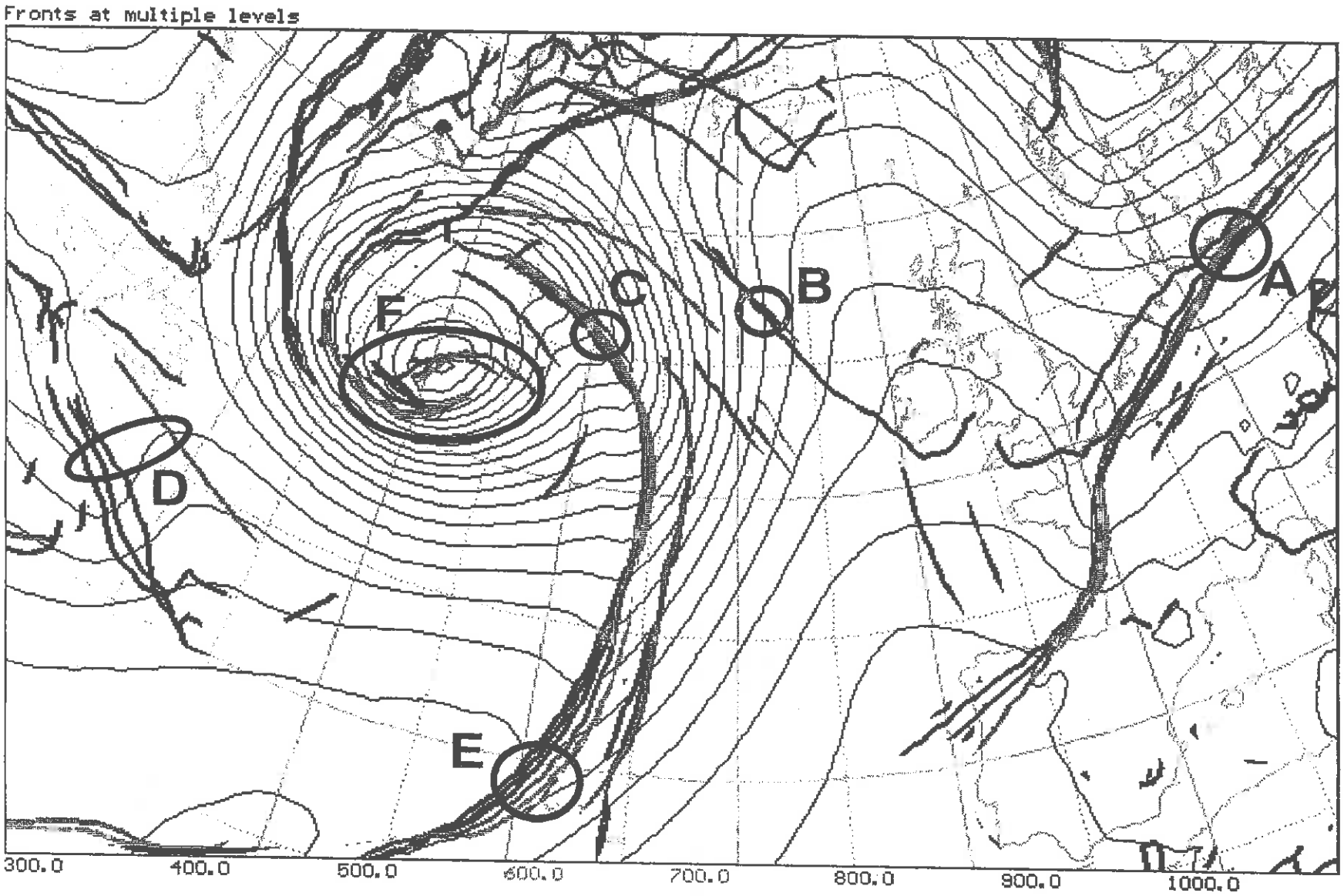

Figure 9: Data is from a LAM analysis for 00UTC, 2nd February 1995 (same as Figures 6 and 7). Thin black lines shows surface pressure at 2hPa intervals. Thick lines show objective θ_w-fronts (equations (6), (9) and (11)) at different pressure levels. Colour signifies pressure level according to the scale below (hPa). Fronts were stacked by working up from 1000hPa . K_1=0.3 and K_2=1.35 have been used at every level.
Labels highlight features referenced in the text.

independent of choice of τ. Here we try using different parameters for τ, and in so doing assess how subjective fronts can best be replicated.

A rigorous dynamical definition of a front would replace τ by potential temperature θ. However atmospheric motion around fronts is generally not dry adiabatic. The main alternative is thus to use a variable such as θ_w or θ_e (equivalent potential temperature) which is essentially conserved during moist ascent and descent, and hence acts as a better airmass tracer. Renard and Clarke (1965) recognised this advantage, but because of the unreliability of the humidity analyses at their disposal retained θ instead. Whilst humidity analyses do still contain errors, they are now much improved.

To evaluate the relative merits of using θ or θ_w a trial front inter-comparison was performed. This covered, retrospectively, a period of approximately one month, beginning mid-January 1995, in 6-hour intervals. The domain used was the same as in earlier examples. A mobile, cyclonic, westerly type was dominant during the period. The trial involved comparing subjectively-analysed surface charts (produced previously by forecasters in the U.K. Met. Office in Bracknell - see example in lower right panel of Figure 10) with composite objective θ-/θ_w-front plots (see example in lower left panel of Figure 10) which had been generated as follows:

1) Compute, from model-analysed fields, the diagnostics in equations (6), (9), (11) and (12) for $\tau=\theta$
2) Repeat step (1) for $\tau=\theta_w$
3) Use the methodology given in Sections 4.1 and 4.2 to plot each type of front (self-consistent sets of masking constants were used here, one set for the θ-fronts and one set for the θ_w-fronts; these had been derived as described in Appendix III).
4) Overlay the plots generated in step (3).

Two series of composite plots were in fact produced - one for 900hPa, to represent surface fronts, and one for 600hPa, to represent upper fronts. The results from the inter-comparison are summarised below:

I) At both 900hPa and 600hPa the majority of θ-fronts have a counterpart θ_w-front (as on Figure 10).

II) The mean distance between θ-fronts and their counterpart θ_w-fronts was 50km at 600hPa and 20km at 900hPa (the positional correlation of the two types of front on Figure 10 (lower left panel) is fairly typical for 900hPa). The larger mean distance at the higher level is due to there being much greater variation in relative humidity at this level.

III) Label 'A' on the top left panel of Figure 10 highlights a type of (warm) θ_w-front which was observed many times; mainly at 900hPa, but also, occasionally, at 600hPa. It denotes the leading edge of the 'warm conveyor-belt flow' found ahead of many marine cold fronts (see Browning (1990)). Out of 219 occurrences of cold θ_w-fronts in the domain 10°W-40°W, 40°N-60°N, 121 (=55%) had some indication of a warm conveyor belt (θ_w-)front ahead of them. Such fronts generally advanced at a similar speed to the companion cold θ_w-front. Note also that there is no counterpart warm θ-front. This was almost always the case, indicating that the implied cross-front change in θ_w denotes a change in relative humidity rather than temperature.

IV) Label 'B' on the top right panel of Figure 10 highlights a type of (cold) θ-front (hugging the Spanish coastline) which was also observed many times, immediately downwind of orography. Such fronts were mostly only seen at 900hPa, but some appeared, additionally, at 600hPa. This (cold) θ-front is caused by the Foehn effect. Such fronts were stationary and persistent, and never appeared to have a counterpart θ_w-front. The absence of a counterpart θ_w-front is consistent with the Foehn effect.

V) As on Figure 10, there was generally quite a good agreement between hand drawn (surface) fronts and both surface θ_w- and surface θ-fronts, and no systematic displacement errors were apparent. This accords with requirement (iii) in section 1.

VI) Hand-drawn surface fronts seemed to occur more frequently than objective surface fronts in the vicinity of the U.K., but less frequently over the northwest of the domain. This is probably because the (U.K.) analysts tend to concentrate on the U.K. area.

VII) On occasions surface fronts on the

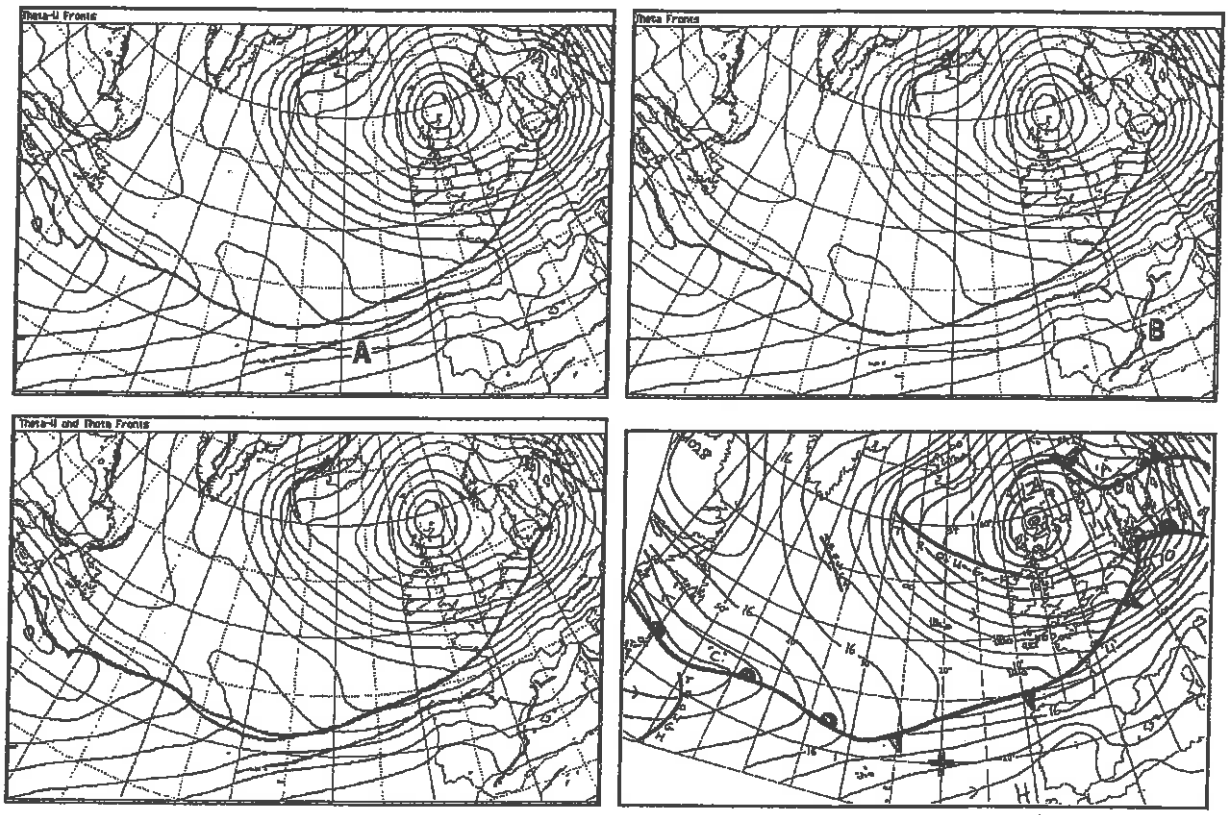

Figure 10: All panels show surface fronts for 00UTC on 23 January 1995, with isobars at 4hPa intervals. Warm fronts are red or magenta, cold fronts blue or cyan. *Lower right panel* is the U.K. Met Office operational surface analysis. *Top left panel* shows objective θ_w fronts derived from a model analysis for 900hPa (K_1=0.3, K_2=1.35); *top right panel* shows objective θ fronts from the same analysis (K_1=0.33, K_2=1.49). *Lower left panel* is a composite of the top two panels, with θ fronts plotted on top. Label 'A' highlights a 'warm conveyor belt front', whilst label 'B' highlights a 'Foehn effect front' (see text for further explanation).

hand-drawn analysis coincided with upper θ-fronts and upper θ_w-fronts, but had no objective counterparts at the 900hPa level. Such occasions were often cold front situations, with a returning polar maritime airmass behind the front. This suggests that differential cross-front surface fluxes had managed to reduce thermal gradients at low levels more than at upper levels. Similarly, forecasters producing manual analyses will often position (surface) fronts in the vicinity of cloud bands they see on imagery, and these bands will often be more closely related to upper fronts than to surface fronts.

The main conclusion to draw from the above results is that either θ or θ_w could be used as the thermal parameter τ. In so far as achieving agreement with hand-drawn analyses is concerned, each parameter has one principal disadvantage; 'warm conveyor belt fronts' are commonly observed when using θ_w (item (III)), whilst 'Foehn effect fronts' are commonly observed when using θ (item (IV)). 'Warm conveyor belt fronts' were inferred to denote a change in relative humidity. It could thus be argued that although not signifying a temperature change, they could have practical value in signifying the onset of a different weather type - ie those conditions which characterise warm conveyor belt flows (e.g. dampness, cloudiness, poor visibility, strong low-level winds, considerable orographic precipitation). Perhaps then raw θ_w-fronts have greater practical value than do raw θ-fronts. Their use would also accord with operational practice in the U.K. Met. Office, where forecasters frequently use model 850hPa θ_w fields (as opposed to θ fields) to help locate surface fronts.

'Warm conveyor belt fronts' can quite often be eliminated, automatically, from a θ_w-front display using *additional* masking, this additional masking being the same as the standard masking used for θ-fronts. The same type of approach could in principle be used to remove 'Foehn effect fronts' from a θ-front display.

In subsequent examples we use $\tau=\theta_w$ in (6) for our front locator, and just the two standard masking variables ((9) and (11)), also with $\tau=\theta_w$.

6 Further Development - the use of Colour

Different frontal characteristics can be easily highlighted by utilising different colouring variables (panel E on Figure 2). In this section we propose some diagnostics to use as colouring variables, and illustrate how plots produced using such variables can provide a greatly enhanced description of frontal structure. These embellishments are not merely cosmetic; they also have predictive value in forecasting (as will be demonstrated) and considerable investigative potential in research.

6.1 Colour schemes

The 'colouring' scheme one chooses to use should generally relate in a clear, intuitive way to the parameter(s) being represented. A very simple two-colour scheme for discriminating between cold and warm fronts was discussed earlier (figure 11a shows an example). Two more general 'incremental' schemes that could be used are these: a *grey series* based on graded shades of grey (for monochrome output), and a *standard colour series* based on the spectrum blue-green-yellow-orange-red.

One benefit of using a colour series is that it allows precise values of the colouring variable to be read off. Another benefit is that a physically significant change in value can be linked to an 'abrupt' change of colour. For example, the boundary between negative and positive could be signified by a change from green to orange (as on many panels in Figure 11).

When selecting the orientation of a particular colour scheme, the objective will usually be to make the active features most prominent. This means that if a colour series is being used red should represent the active end of the scale, whilst if using a grey series on a white background the darkest shade of grey should do likewise.

6.2 Frontal intensity

Two natural colouring variables to use to indicate frontal intensity, or activity, are vorticity and relative humidity (see Huber-Pock and Kress (1981) and (1989) for further discussion). The former is a simple dynamical indicator, the latter an indicator of cloud extent.

The two left hand panels of Figure 11b show colour examples, in which reds signify larger values. The two most active frontal regions are clearly associated with wave depressions A and C (labelled on Figure 11a). Conversely the fronts over Norway, Spain and central Europe appear weak and insignificant. The lower left panel also suggests that cloud associated with the cold front south of low A is limited to low levels.

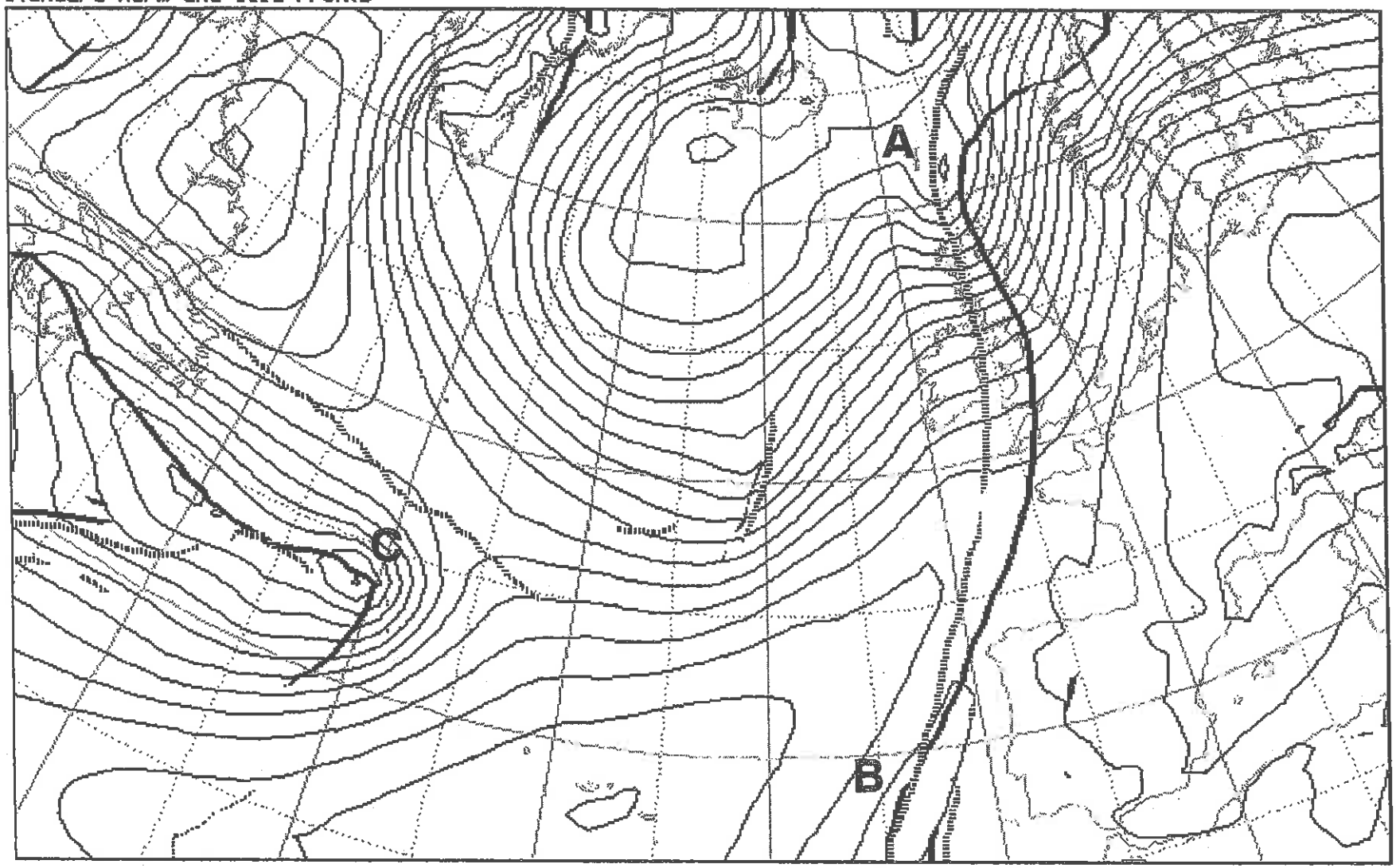

Figure 11a: Data is from a 12-hour LAM forecast for 12UTC on 9th October 1995. Black lines show surface pressure at 2hPa intervals. Coloured lines show surface (900hPa, solid) and upper (600hPa, broken) warm (red) and cold (blue) objective θ_w-fronts (equations (6), (9), (11) and (12)). K_1=0.3 and K_2=1.35 were used for surface fronts, and K_1=0.3 and K_2=0.9 for upper fronts.

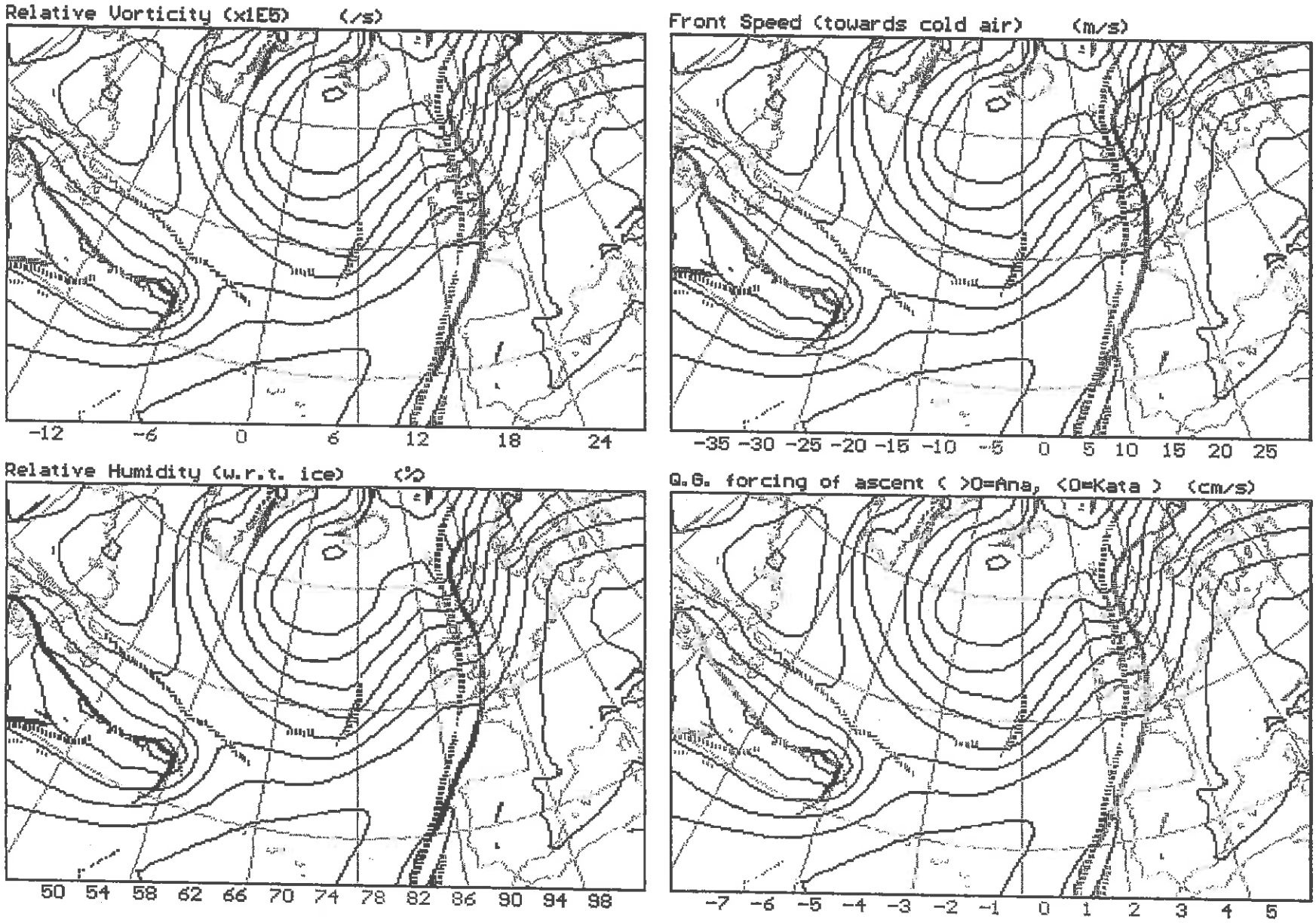

Figure 11b: Data is from a 12-hour LAM forecast for 12UTC on 9th October 1995 (same as Figure 11a). Black lines show surface pressure at 4hPa intervals. Fronts are coloured according to values of particular (colouring) variables at the respective surface (900hPa, solid) and upper (600hPa, broken) levels;
Top left panel shows relative vorticity ($x10^{-5}s^{-1}$), *top right panel* front speed towards cold air (ms^{-1}), *lower left panel* relative humidity (%) and *lower right panel* ω_{QG} (cms^{-1}) (also see text).
Scales beneath panels represent values of the colouring variables (numbers show the lower limit of a colour's range).

Recall also that to a first approximation (geostrophic) relative vorticity, as depicted in the top left panel of Figure 11b, is proportional to the frictionally-induced component of the vertical motion (ω_{fr}) at the top of the boundary layer (see Holton (1992), chapter 5). ω_{fr} can be sufficiently large to contribute substantially to the generation of surface precipitation. For example, if the low level geostrophic relative vorticity were of order 2f (as represented, approximately, by red on Figure 11b) then condensation in the boundary layer which had been triggered solely by ω_{fr} would be sufficient, in itself, to produce a rainfall rate of order 0.2mm/hr (averaged over the cross-front distance across which the vorticity had been computed - this is 200km on Figure 11b).

6.3 Front speed

The objective here is to colour in fronts according to their speed of movement. In this study fronts have been plotted as contours (of a field Ψ), so front speed will be given by the speed of movement of these contours in a perpendicular direction (call $V_{\Psi contour}$). Assuming that contours are advected with the wind, then $V_{\Psi contour}$ is simply given by

$$V_{\Psi contour} = \mathbf{V}\cdot\nabla\Psi / |\nabla\Psi|$$

Rather than use the diagnostic quantity in (6) to replace Ψ, and probably introduce noise when a further derivative is calculated, a better alternative is to approximate the orientation of front contours by contours of $|\nabla\tau|$ (see figure 5). Then the front speed of movement in a perpendicular direction (V_{front}) is simply given by:

$$V_{front} = \mathbf{V}\cdot\nabla|\nabla\tau| / |\nabla|\nabla\tau|| \qquad \cdot(13)$$

The top right panel of Figure 11b is an example; the colours signify the speed of movement towards the *cold air side* of the front.

Aside from giving a direct readout of front speed, plots such as this also allow relative front motion to be assessed. For example the upper cold front just south of low A is apparently moving faster than the surface front (on account of slightly darker blue shades) and therefore may subsequently overrun (to generate a 'split cold front', as in the model of Browning and Monk (1982)). The frontal slope in this forecast run did in fact become steeper at later times. There is also a suggestion that the surface front just north of low B is moving slowly west-northwest, whilst the upper front edges east-southeast. Such relative motion will tend to destabilise the atmosphere, and convective precipitation may ensue.

6.4 Ana-fronts and Kata-fronts

The Meteorological Glossary (Meteorological Office (1991)) states that fronts can be categorised as ana-fronts or kata-fronts according to whether air on the warm air side of the frontal zone - ie in the vicinity of the front itself - is ascending (ana-front) or descending (kata-front). By computing a diagnostic quantity which represents the vertical motion at a particular level, then using that quantity as a colouring variable for fronts derived for that level, one can signify whether ascent or descent are being forced to occur along particular front segments, and thus whether these segments have ana- or kata-characteristics. It will be convenient to assume here that the primary determinant of vertical motion around fronts is *quasi-geostrophic* forcing. This is not unreasonable given that quasi-geostrophic dynamics underpin many theories of vertical motion in the atmosphere.

The geostrophically-forced part of the vertical motion (call $\omega_{QG}(x,y,p)$) can be computed by solving the omega equation as discussed by Clough et al (1994). Here we present an example, in which $\omega_{QG}(x,y,p=900hPa)$ and $\omega_{QG}(x,y,p=600hPa)$, thus derived, have been used as colouring variables for surface fronts and upper fronts respectively (lower right panel of Figure 11b). Note that orange and red denote ana- characteristics, and green and blue kata-characteristics.

On this example most of the warm fronts clearly have strong ana- characteristics, particularly the front ahead of low C. Wherever strong ana- characteristics are associated with high humidity (lower left panel), thick cloud and precipitation are to be expected. And as indicated in section 6.2 precipitation will be further enhanced (by ω_{fr}) if there is, additionally, large vorticity at the surface front level, as there is around low C (top left panel).

The upper level front subject to the largest forced ascent (>3 cms^{-1}) is the short (secondary) cold front situated southwest of Ireland. As this lies in a cold, unstable, polar maritime airmass one would expect considerable enhancement of convective activity to result. Indeed many SFERICs were registered close to this front during the next few hours.

The kata- cold front immediately south of low A should be characterised by general descent, and thus only limited precipitation, and

thinning cloud. Whilst an extensive cloud band *was* associated with the front at validity time, animated imagery showed this cloud to dissipate markedly thereafter.

7. Other Products

Here we describe other ways in which objective front plotting can be tailored to meet specific requirements. Figures 12 to 14 are included to illustrate the type of products which can be produced; the intention is not to discuss each meteorological situation in detail.

7.1 Frontal Evolution

When forecasts are being produced for a particular region, the content of those forecasts will depend critically on the time evolution of front locations in and around that region. Such information can be provided to the forecaster as objective front animations, but also in hardcopy form as a composite plot of front isochrones. Such plots can be made intelligible by labelling the plotted fronts according to the time to which they correspond. This can be achieved with relative ease using a standard contour labelling facility.

Figure 12 shows an example 'frontal evolution' plot, for surface fronts, which was produced automatically. Labelling corresponds to the time, in hours, after data time. Plots such as this can initially seem confusing, but this is largely due to unfamiliarity. Many features (such as acceleration, pivoting and frontal waves) produce their own distinctive patterns, and with experience such patterns can be recognised quite readily.

There are two substantial features depicted on Figure 12. One is a cold front tracking southeast across Scotland, pivoting around a point west of Ireland. The second is a cold front tracking southwest from Denmark; the cold continental air to its rear encroaches into the far southeast of England, but then the front slows down as milder maritime air begins to push in from the northwest (shown as a warm front over the southeast of the North Sea).

7.2 Composited data

One of the aims of producing objective front plots was to provide the forecaster who has to draw up surface charts (such as that shown in the lower right panel of Figure 10) with an on-screen first-guess front field that they could subsequently modify. The composite plots in Figures 13 and 14 are examples of the types of product which could help with this modification (as is Figure 11b). On these plots the objective fronts (shown in thick black on Figure 13 and in conventional colours on Figure 14) are combined with examples of *secondary* frontal characteristics (see section 2), which would form the basis for the modifications. Secondary characteristics fall into two categories; those that are model-generated, which would be used for producing a forecast chart (as on Figure 13, which uses a 36-hour forecast), and those that are 'observed', which could be used to produce an analysis chart (as on Figure 14). Note that figures 13 and 14 have the same validity time, and can thus be compared. The secondary characteristics shown include precipitation (in grey on Figure 13, and in green on Figure 14), layer mean tropospheric temperature (coloured thickness lines on Figure 13) and cloud pattern (grey-scale on Figure 14).

It is envisaged that the primary rôle of the forecaster would be to delete those fronts they considered non-significant, but on occasions they might also move or possibly add fronts. Considering the example depicted in Figures 13 and 14, some of the fronts in the northwestern corner of the domain could be considered to be too incoherent, and to not have a sufficient cloud/vorticity signature to be retained. Nevertheless a few of these fronts were associated with maxima in the model-derived precipitation forecast (Figure 13), and should perhaps not be deleted.

Whilst it is uncommon to see short fronts plotted operationally, short objective fronts are relatively common. It is easy to dismiss these as spurious/incorrect. However inspection of plots such as Figure 14 over a period of months has shown that short fronts present in the U.K. radar network area (see black outline on Figure 14) are often associated with short, coincident mesoscale precipitation bands, and thus not easily dismissed. On Figure 14 the organised areas of precipitation just northwest of the U.K. and just southeast of the U.K. are probably related to short upper warm fronts nearby. Similarly the short surface warm front shown close to the French Riviera was associated with flooding in that region. In general short fronts seem to not be as long-lived as larger-scale fronts, but they can often be tracked over many hours.

There are further applications of plots which show objective fronts overlaid on other data. For example, including *observational* data, as on Figure 14, can help forecasters to identify model

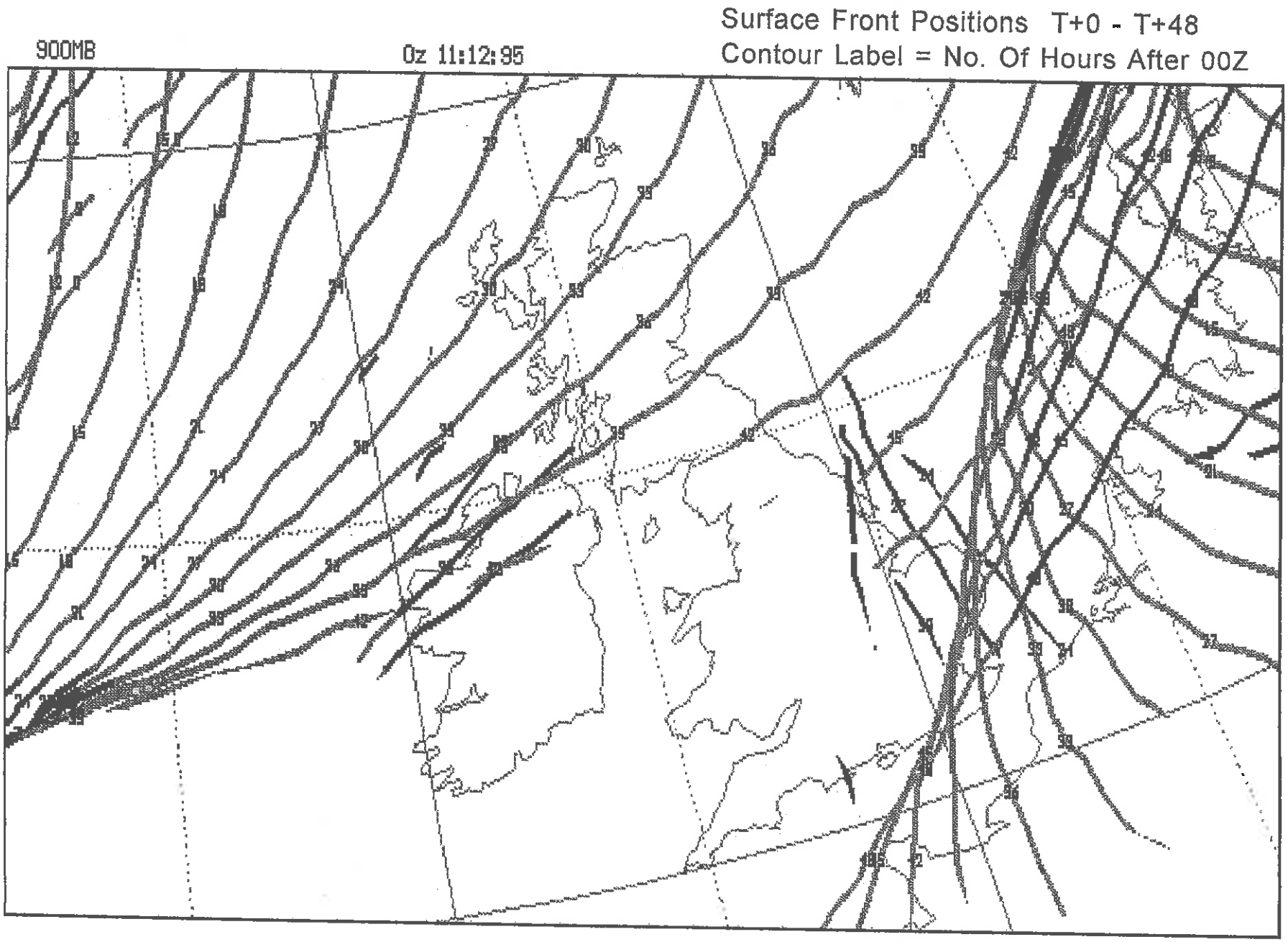

Figure 12: Composite plot showing forecast evolution of objective surface θ_w-fronts between 00UTC on 11th and 00UTC on 13th December 1995 (K_1=0.3 and K_2=1.35). Uses a LAM forecast with a data time of 00UTC on 11th. Labelling signifies number of hours after data time that a front corresponds to.

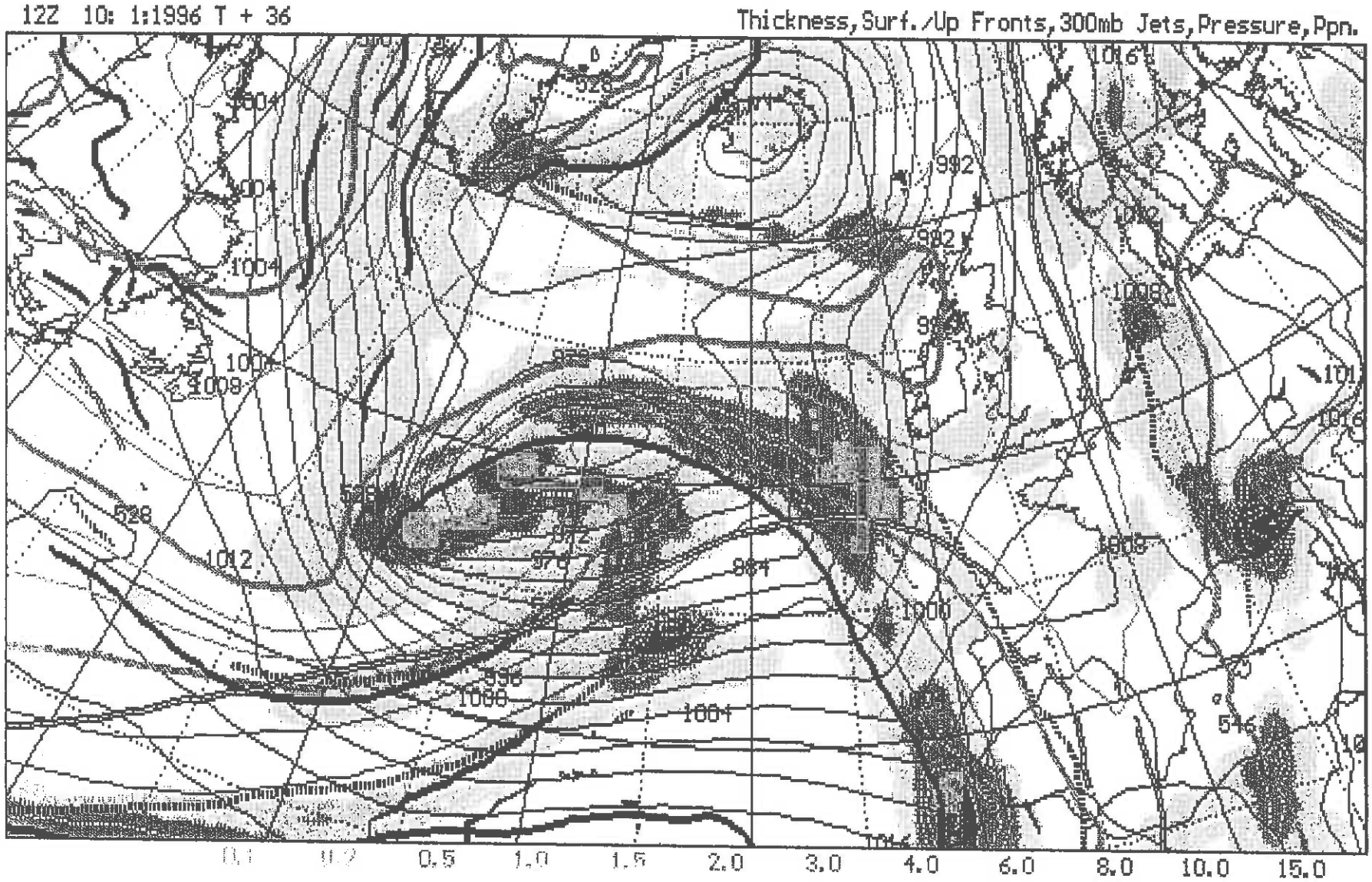

INSERT FIG 13

Figure 13: Composite *forecast* plot for 12UTC on 10 January 1996. Uses a 36-hour LAM forecast. Thin black lines show surface pressure at 4hPa intervals. Thick black lines show objective θ_w-fronts for the surface (solid, 900hPa, K_1=0.3 and K_2=1.35) and upper levels (broken, 600hPa, K_1=0.3 and K_2=0.9). Black/white 'tracks' show jet cores >40ms^{-1} at 300hPa. Grey shading/broken white contours show total precipitation rate (mmhr^{-1}); lightest shade begins at 0.05, then contours for every value on the scale below. Coloured lines show 1000-500hPa thickness, at 6dm intervals.

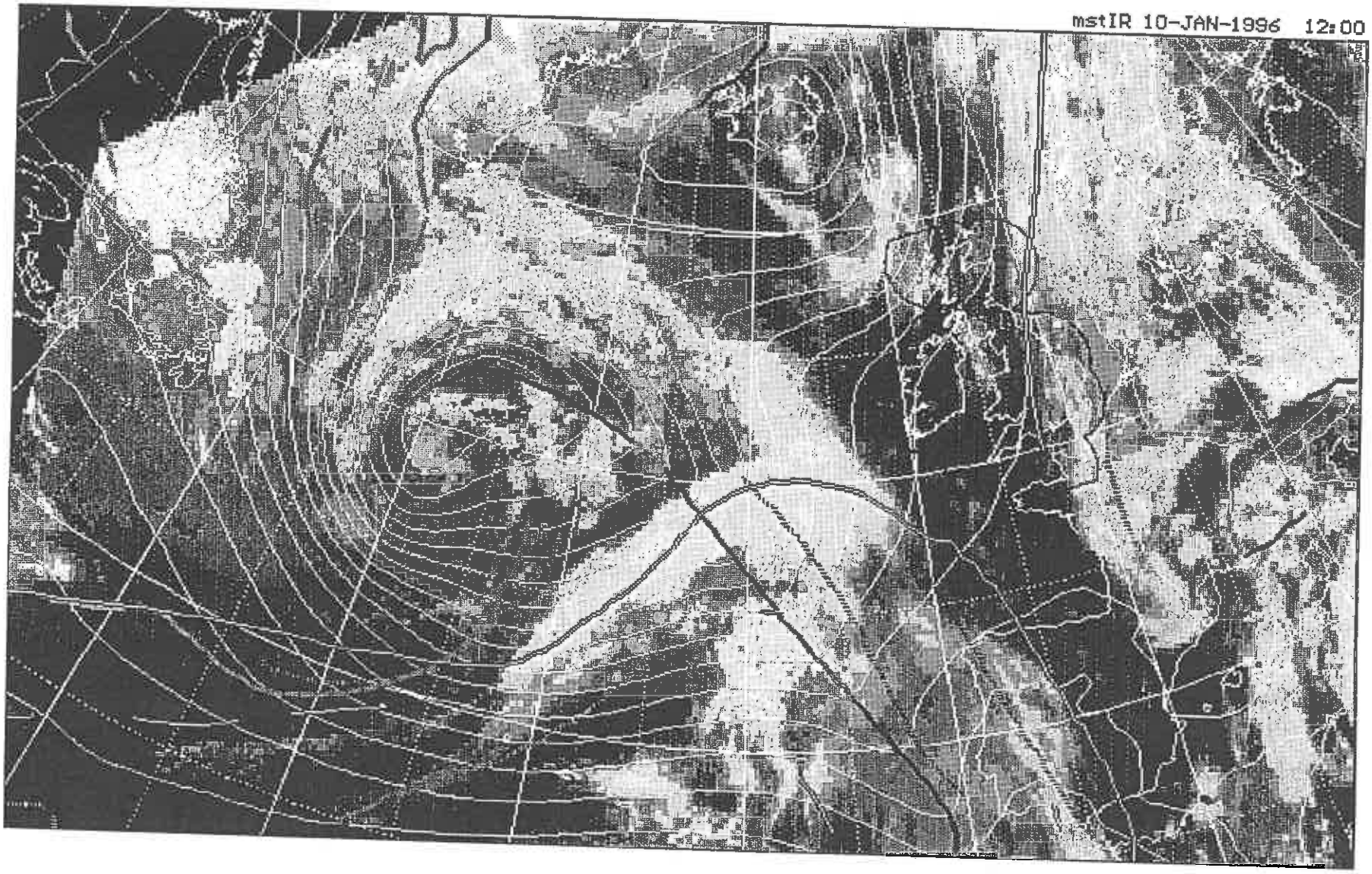

Figure 14: Composite *analysis* plot for 12UTC on 10 January 1996. Uses a LAM analysis and observations. Yellow lines show surface pressure at 4hPa intervals. Thick red/blue lines show objective θ_w-fronts for the surface (solid, 900hPa, K_1=0.3 and K_2=1.35) and upper levels (broken, 600hPa, K_1=0.3 and K_2=0.9). Black/white 'tram lines' show jet cores >40ms^{-1} at 300hPa. Background image is Meteosat infra-red. Green shows precipitation rates>0.05mmhr^{-1}, from the U.K radar network (delimited in black). Pink dots/squares are SFERICS reports between 0930 and 1330UTC.

INSET FIG 14

errors. Composited images also provide a powerful research tool, particularly when consecutive times are combined into animations. Such animations are very useful for studying system evolution.

8. Summary and concluding discussion

This paper has demonstrated how mathematical and graphical techniques can be combined together to enable atmospheric fronts to be plotted on a computer screen without human intervention. A thorough search of the meteorological literature suggested that progress in this field had hitherto been very limited.

The objective front-plotting system requires as its' primary input a gridded dataset for one thermodynamic variable. Such data would generally be extracted from an analysis or a forecast of a numerical model. The input data is manipulated to produce other derived variables which facilitate the front-plotting.

As a graphical entity a front constitutes a line segment. Line segments representing fronts are drawn on-screen by first contouring a value zero for one derived field (the *locating* variable), and by then erasing portions of these contours according to the values of two other derived fields (the *masking variables*). The primary challenge has been devising appropriate locating and masking variables; their definitions are given in (6), (9), (10) and (11) in section 5.3. Another key task was found to be selecting appropriate finite differencing techniques to evaluate the diagnostics.

The masking variables represent the 'thermal gradient in the adjacent baroclinic zone' and the 'cross-front rate of change of thermal gradient'. The user can adjust the thresholds associated with each of these, thereby 'tuning' their output. Lower thresholds lead to a greater total front length. Threshold values which give a total front length similar to that seen on subjective analyses have been proposed for two different thermal parameters. The thresholds were derived for a North Atlantic region during a winter period; if dynamical consistency is to be maintained then the same values should be used for other regions, and probably also for other seasons. However the quoted values apply specifically to data with a gridlength of 100km - for smaller gridlengths they would increase.

The question as to what thermodynamic variable one should use was also addressed. θ and θ_w were considered, and a systematic evaluation of their merits performed. Frequently differences in frontal positioning were small. Both θ and θ_w had advantages, but it was concluded that θ_w-fronts were generally the more useful. Objective θ_w-fronts were usually less than one fifth of a grid spacing away from where a subjective analyst would have placed them using just the θ_w field. Partly because of this, the differences between the positions of objective θ_w-fronts and subjective 'operational' fronts were also generally small. This was in spite of the fact that subjective analyses drawn by different analysts usually differ slightly (when they use the same data).

There are several meteorological fields in which one would want to utilise objective front plotting; notably forecasting, research and aviation. In forecasting it is envisaged that the forecaster would use objective fronts as an 'on-screen first-guess field', which could be slightly modified in the light of other model or observational data. The requirement in research is perhaps slightly different; here dynamical consistency should perhaps be retained by leaving the objective fronts untouched. In automating the production of the significant weather (SIGWX) chart used in aviation either of these approaches might be used.

The advantages of using objective rather than manual methods to plot fronts are wide-ranging. Because the objective fronts are allied to a precise dynamical definition, they will be wholly self-consistent, both temporally and spatially. There should also be a substantial saving of resources, particularly forecaster time. Front animations can also now be realised. These should be of considerable value in research, facilitating, for example, a much more systematic evaluation of conceptual models than has hitherto been possible.

In the past it has been commonplace to represent different frontal structures by plotting in different ways, the simplest example being distinguishing between warm and cold fronts. Many of these processes can now be automated. In this paper we have proposed several 'colouring schemes' which enable frontal intensity, speed of frontal movement and ana- and kata- characteristics to all be represented objectively. In addition, by plotting fronts at more than one level a 'split-front' structure can also be recognised.

Occlusions are not represented as such by the objective front-plotting method; instead they will usually be plotted as a cold front, as a warm front, or occasionally as a near-parallel cold front-warm front pair. There are other linear

features which can appear on subjectively drawn charts which have not been discussed here, notably trough lines and jet streams. Locating and masking variables which facilitate the plotting of these features have been devised, and will be published in a brief follow-up paper.

The examples presented in this paper are based on pressure-level data and cover what is primarily an oceanic region. Frontal structure in regions of topography, which pressure surfaces intersect, is likely to be more complex. Such structures require further investigation, and will probably be clearer if a terrain-following vertical co-ordinate is utilised instead.

Here at JCMM in Reading objective front plots and animations similar to Figures 11 to 14 have been routinely produced for several months now. It is interesting to note that back in 1965, Carlson et al, in discussing the objective location of frontal zones, prophesied automation, stating that 'synoptic frontal analysis was (then) entering the machine and space age'. Their prognosis, it seems, still applies.

Acknowledgements

This work has benefitted from discussions with Nigel Wood, Doug Parker, Keith Browning, Neil Gimson, Charlie Attwood and Mike Pedder. Sid Clough provided comprehensive reviews of preliminary manuscripts. Phil Brown (SH) assisted with the θ- vs θ_w-front comparison, and Tyrone Fay helped set up product automation.

The Joint Centre for Mesoscale Meteorology is supported by the Meteorological Office and the Department of Meteorology at the University of Reading.

APPENDIX 1

Out of the basic first order quantities which can be computed from a horizontal 2-dimensional vector field (μ) just two are invariant with respect to a rotation of the co-ordinate system. These are the divergence D and the vorticity ξ (vertical component):

$$D = \partial\mu_x/\partial x + \partial\mu_y/\partial y$$
$$\xi = \partial\mu_y/\partial x - \partial\mu_x/\partial y$$

Holton (1992, pages 95, 96) decomposes the vorticity into two constituent parts, which themselves are not invariant under rotation, but both of which can be computed locally. These are the curvature vorticity (ξ_{curv}) and the shear vorticity (ξ_{shear}). They can be expressed according to a local rotated Cartesian co-ordinate system (s,n), where unit vector $\hat{s} = \mu/|\mu|$ is tangential to the local streamline through the μ field (figure A1), as follows:

$$\xi_{curv} = \partial\mu_n/\partial s$$
$$\xi_{shear} = -\partial\mu_s/\partial n$$
$$(\ \xi = \xi_{curv} + \xi_{shear}\ )$$

Saucier (1955) refers to the directions s and n, thus defined, as *kinematic* directions.

Similarly, the divergence can also be decomposed into two constituent parts (Saucier, 1955): the 'stretching term' ($D_{stretch}$) and the 'spreading term' (D_{spread}). In the kinematic co-ordinate system these are written:

$$D_{stretch} = \partial\mu_s/\partial s$$
$$D_{spread} = \partial\mu_n/\partial n$$
$$(\ D = D_{stretch} + D_{spread}\ )$$

If s is replaced by $-s$ and n by $-n$ in each of the equations for ξ_{curv}, ξ_{shear}, $D_{stretch}$ and D_{spread} then the values of these derived quantities will be unchanged (as if using co-ordinates (s',n') on Figure A1). This implies that *in so far as computation of these quantities is concerned* the unit vector $\hat{s}$ should be defined to be *plus or minus* a vector quantity; in other words $\hat{s}$ is in fact a **unit axis**. Such an entity is expressed, in this paper as either $\pm\hat{s}$ or $\hat{s} = \pm\mu/|\mu|$. Similarly, *in*

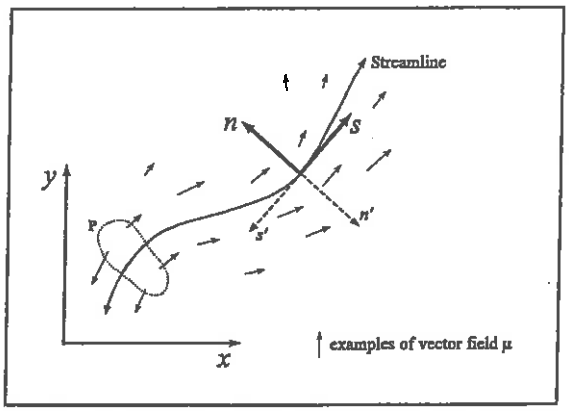

Figure A1: Definition of the local right-handed cartesian co-ordinate system (s,n) for a vector field μ. Spatial derivatives of μ are computed with (s,n) fixed locally, ie with s *tangential* to the local streamline. The co-ordinates (s',n') (shown dashed) and the region marked P are explained in the text.

so far as computation of the aforementioned quantities is concerned, the streamline marked on Figure A1 should be considered continuous through any regions where the vectors reverse direction, such as within the area marked P.

APPENDIX 2

This appendix details how to derive the 'mean' of a set of axes. An 'axis' has a magnitude and an orientation but not a direction; using vector notation it can be expressed as '$\pm\mu$'.

One example of a physically meaningful quantity which is an axis is the 'dilatation axis'. This represents the orientation along which fluid elements in a two-dimensional flow field are being 'stretched out'. It is conventional to plot a dilatation axis such that its length represents the magnitude of the deformation (see, for example, Keyser, Reeder and Reed (1988)).

Sub-section (i) describes a mathematical way of computing the mean of a set of axes and sub-section (ii) a graphical alternative. Simple examples comparing mean axes with mean vectors are given in (iii). Sub-sections (ii) and (iii) are included to enable the reader to visualise what is implied by the term 'mean axis'.

(i) Mathematical solution

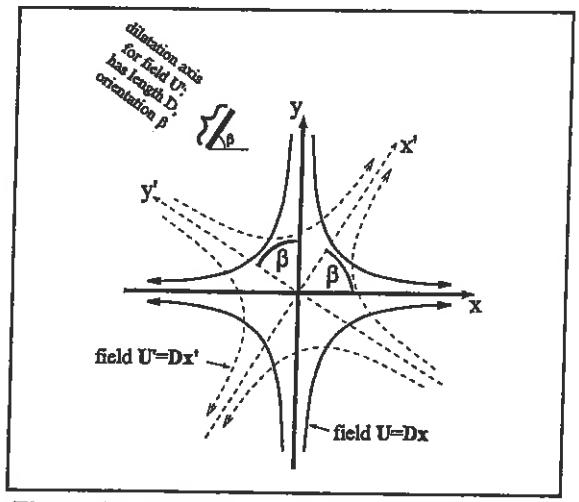

Figure A2: Schematic representing 2 two-dimensional fields of pure deformation. Solid lines relate to a field whose dilatation axis (not shown) is parallel to the x-axis; dashed lines relate to a field whose dilatation axis (shown) is parallel to the axis x'. Co-ordinate transformation from (x',y') to (x,y) involves a clockwise rotation, about the origin, through angle β.

Consider the set of n axes defined as (D_i,β_i) for i=1 to n, where D_i is the magnitude/length of an axis (≥ 0) and β_i its orientation ($0° \leq \beta_i \leq 180°$). Each such axis can be considered to be the dilatation axis of a separate two-dimensional pure deformation (vector) field. Each such field can be expressed as:

$$U_i' = D_i x_i'$$
$$V_i' = -D_i y_i'$$

where the prime symbol denotes a cartesian co-ordinate system rotated anti-clockwise about the origin through β_i, such that its x-axis lies parallel to the dilatation axis of field i (Figure A2).

In matrix notation the above equations can be re-written as:

$$\underline{U_i'} = D_i \, \underline{x_i'} \qquad \text{(A2.1)}$$

where $\underline{U_i'} = \begin{bmatrix} U_i' \\ V_i' \end{bmatrix}$, $D_i = \begin{bmatrix} D_i & 0 \\ 0 & -D_i \end{bmatrix}$, $\underline{x_i'} = \begin{bmatrix} x_i' \\ y_i' \end{bmatrix}$

The mean of all the axes (D_i,β_i) will be given by (D_{mean},β_{mean}) where (D_{mean},β_{mean}) defines the ('resultant') dilatation axis for the respective deformation (vector) fields summed together, and thence averaged, ie for U_{mean} where:

$$U_{mean} = \frac{1}{n} \sum_{i=1}^{n} U_i \qquad \text{(A2.2)}$$

To perform the summation each deformation (vector) field will first be re-expressed in standard cartesian co-ordinates (x,y). Referring to Figure A2 note that:

$$\underline{x_i'} = R \, \underline{x_i}$$
$$\text{and} \qquad \underline{U_i'} = R \, \underline{U_i} \qquad \text{(A2.3)}$$

$$\text{where} \qquad R = \begin{bmatrix} \cos(\beta_i) & \sin(\beta_i) \\ -\sin(\beta_i) & \cos(\beta_i) \end{bmatrix}$$

Substituting A2.3 into A2.1 gives:

$$R \, \underline{U_i} = D_i \, R \, \underline{x_i}$$
$$\therefore \quad R^{-1} R \, \underline{U_i} = R^{-1} D_i \, R \, \underline{x_i}$$
$$\therefore \quad \underline{U_i} = R^{-1} D_i \, R \, \underline{x_i}$$

Then evaluating $R^{-1} D_i R$ gives:

$$U_i = \begin{bmatrix} D_i\cos(2\beta_i) & D_i\sin(2\beta_i) \\ D_i\sin(2\beta_i) & -D_i\cos(2\beta_i) \end{bmatrix} x_i \qquad \cdot(A2.4)$$

Thus from A2.2:

$$U_{mean} = \frac{1}{n} \begin{bmatrix} \sum_{i=1}^{n} D_i\cos(2\beta_i) & \sum_{i=1}^{n} D_i\sin(2\beta_i) \\ \sum_{i=1}^{n} D_i\sin(2\beta_i) & -\sum_{i=1}^{n} D_i\cos(2\beta_i) \end{bmatrix} x_i$$

Then substituting:

$$P = \sum_{i=1}^{n} D_i\cos(2\beta_i) \;, \qquad Q = \sum_{i=1}^{n} D_i\sin(2\beta_i)$$

gives:

$$U_{mean} = \frac{1}{n} \begin{bmatrix} P & Q \\ Q & -P \end{bmatrix} x_i$$

Direct analogy with A2.4 implies that:

$$\frac{P}{n} = D_{mean}\cos(2\beta_{mean})$$

and $$\frac{Q}{n} = D_{mean}\sin(2\beta_{mean})$$

Thus:

$$\beta_{mean} = \frac{1}{2}\tan^{-1}\left(\frac{Q}{P}\right) \qquad \cdot(A2.5)$$

and $$D_{mean} = \frac{1}{n}\sqrt{P^2 + Q^2} \qquad \cdot(A2.6)$$

(ii) Graphical solution

A precise but relatively simple graphical method for deriving the mean of a set of axes follows on directly from equations A2.5 and A2.6. This is illustrated in Figure A3. The steps required are these (numbers refer to figure labels):

(1) Start with n axes (n=3 in this example).

(2) Plot the axes on a Cartesian grid, with their ends at the origin. Measure the angle each makes with the +ve x-axis.

(3) Double the angles derived in (2); replot each axis as a vector.

(4) Sum the vectors; plot the resultant. Measure the angle the resultant makes with the +ve x-axis.

(5) Halve the angle measured in (4); replot.

(6) Multiply vector length by 1/n (1/3 here); replot as an axis.

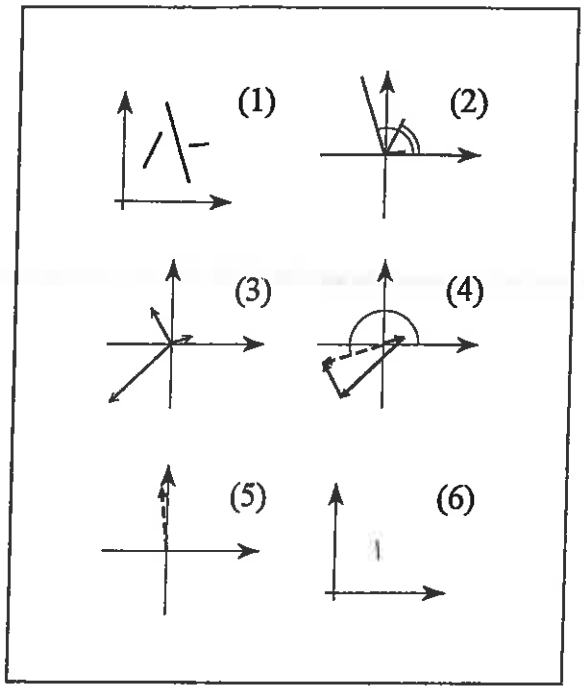

Figure A3: Steps required to compute the 'mean' of a set of n axes. In this example n=3 (panel (1)). The resultant mean axis is shown in panel (6). The steps are described in the text.

Thus the 'mean' of the three axes shown at (1) is deduced to be the axis shown at (6).

(iii) Mean axes and mean vectors

Figure A4 shows simple examples of pairs of vectors (top row), together with the 'mean' of

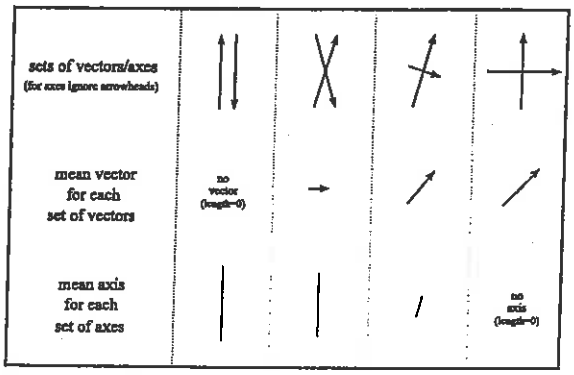

Figure A4: Simple examples showing a 'mean vector' and a 'mean axis' derived from each of for four different pairs of vectors/axes.

each such pair (middle row). These mean vectors can be compared with respective 'mean axes' (bottom row). In deriving the mean axes the initial vector pairs were treated as axis pairs - ie as if no arrowheads existed. Clearly the orientation (and magnitude) of a mean vector can differ greatly from the orientation (and magnitude) of the corresponding mean axis.

APPENDIX 3

This appendix describes how the standard masking constants to be used for plotting θ_w-fronts and θ-fronts were initially derived. θ_w-fronts were considered first.

(i) θ_w-fronts

In selecting values to use for masking constants for θ_w-fronts there were seen to be two primary goals. The first was to match the average 'total front length' on the objective front output to the average 'total front length' observed on operational subjective (surface) analyses which covered the same area. The second goal was then to obtain the best agreement, in terms of location, between the objective and the subjective fronts. Model forecasts and analyses were examined on most days during a 10 month trial period, and by a process of 'manual iteration' it gradually became apparent what level of values would produce the 'best' fronts. It is acknowledged that this 'manual iteration' is imprecise. In particular there were problems dealing with occlusions, which are not represented as such in the objective method, and 'warm conveyor belt fronts'. Nevertheless, workable values were obtained:

600hPa: $K_1 = 0.3$, $K_2 = 0.9$

900hPa: $K_1 = 0.3$, $K_2 = 1.35$

These apply to model data with a gridlength of ~100km; K_1 is in units of °C per 100km per 100km, and K_2 in units of °C per 100km.

Lower thresholds tend to be required at higher levels (to produce a similar total front length) because at these higher levels, where temperatures are generally lower, changes in relative humidity have a smaller impact on θ_w. It might be expected that the thresholds would also vary according to time of year (ie lower during summer). However evidence to date suggests the magnitude of any such annual cycle should be small (say ~10%).

(ii) θ-fronts

Once appropriate values for K_1 and K_2 had been found for θ_w-fronts, counterpart masking constants for the θ-fronts were calculated as follows:

$$(K_1,K_2)_{\tau\text{-}\theta,P\text{-}900mb} = [(\partial\theta/\partial\theta_w)_{RH\text{-}100\%,P\text{-}900mb}]\,(K_1,K_2)_{\tau\text{-}\theta_w,P\text{-}900mb}$$

$$(K_1,K_2)_{\tau\text{-}\theta,P\text{-}600mb} = [(\partial\theta/\partial\theta_w)_{RH\text{-}100\%,P\text{-}600mb}]\,(K_1,K_2)_{\tau\text{-}\theta_w,P\text{-}600mb}$$

This gave:

600hPa: $K_1 = 0.47$, $K_2 = 1.41$

900hPa: $K_1 = 0.33$, $K_2 = 1.49$

In deriving the thermodynamic ratios $(\partial\theta/\partial\theta_w)$ a temperature structure considered to represent ambient (winter-time) conditions over the domain had been assumed (ie θ_w in the range 0 to 10°C). Although a saturated atmosphere was also assumed, the ratios differ only slightly for drier air; e.g. for RH=70% they are about 10% larger. Thus from a thermodynamic standpoint the set of masking constants used for θ-fronts should have been reasonably consistent with the set of masking constants used for θ_w-fronts.

(n.b. Winter-time conditions had been assumed because it was over a winter period that the trial comparison between θ-fronts and θ_w-fronts was performed).

References

Bishop, C.H. and Thorpe, A.J. 1994. Frontal wave stability during moist deformation frontogenesis. Part 2: the suppression of non-linear development. *J. Atmos. Sci.*, **51**.

Bjerknes, J. and Solberg, H. 1922. Life cycles of cyclones and the polar front theory of atmospheric circulation. *Geofys. Publ.*, **3**, no. 1, 1-18.

Browning, K.A. 1990. Organization of clouds and precipitation in extratropical cyclones. Pp 129-153 in *Extra-tropical cyclones: Erik Palmén Memorial Volume.* Eds C. Newton and E. O. Holopainen, American Meteorological Society, Boston, Mass.

Browning, K.A. and Monk, G.A. 1982. A simple model for the synoptic analysis of cold fronts. *Q.J.R.Meteorol.Soc.*, **108**, 435-452.

Browning K.A. and Roberts, N.M. 1994 Structure of a frontal cyclone. *Q. J. R. Met. Soc.* **120**, 1535-1557.

Cahir, J.J. and Lottes, W.D., 1982. An objective diagnostic aid in locating meteorologically significant boundaries. In Preprints of 9th Conference on Weather Forecasting and Analysis, Seattle, Washington, June 28-July 1, 1982. American Meteorological Society, Boston. 296-299.

Carlson, P.E., Galloway, J.L. and Haering P.C. 1966. A Note on the Objective Location of Frontal Zones. *Meteorol. Mag.* **95**. 218-219.

Clarke, L.C. and Renard, R.J. 1966. The U.S. Navy Numerical Frontal Analysis Scheme: Further Development and a Limited Evaluation. *J. Appl. Met.*, **5**, 764-777.

Clough, S.A., Davitt, C.S.A. and Thorpe, A.J. 1996?. Attribution concepts applied to the omega equation. *Q. J. R. Met. Soc. to appear shortly.*

Heimann, D. 1990. 3-dimensional modelling of synthetic cold fronts approaching the Alps, *Meteorol. Atmos. Phys.*, **47**, 197-219.

Heimann, D. 1992a. 3-dimensional modelling of synthetic cold fronts interacting with northern alpine foehn, Meteorol. Atmos. Phys., **48**, 139-163.

Heimann, D. 1992b. Potential and equivalent-potential temperature patterns at cold fronts with prefrontal Foehn. *Meteorol. Atmos. Phys.*, **48**, 165-171.

Holton, J. R. 1992. An Introduction to Dynamic Meteorology. Academic Press, London.

Huber-Pock, F. and Kress Ch., 1981. Contributions to the problem of numerical frontal analysis. Proceedings of the Symposium on Current Problems of Weather-Prediction. Vienna, June 23-26, 1981. Publications of the Zentranstalt fur Meteorologie und Geodynamic 253.

Huber-Pock, F. and Kress, Ch., 1989. An Operational Model of Objective Frontal Analysis based on ECMWF Products, *Meteorol. Atmos. Phys.*, **40**, 170-180.

Hoinka, K.P. and Volkert, H. 1992. Fronts and the Alps - findings from the front experiment 1987. *Meteorol. Atmos. Phys.*, **48**, 51-75.

Kirk, T.H., 1965. A parameter for the objective location of frontal zones. *Meteorol. Mag.*, **94**, 351-353.

Japan Meteorological Agency, Tokyo. 1988. On the improvement of the significant weather chart. Weather Serv. Bull. 55, no. 1. 16 pages.

Mass, C., 1991. Surface synoptic analysis: Time for a reassessment? *Bull. Amer. Meteor. Soc.*, **72**, 348-363

Meteorological Office. 1991. Meteorological Glossary. London. HMSO.

Monk, G.A. 1992. Synoptic and mesoscale analysis of intense mid-latitude cyclones. *Meteorol. Mag.*, **121**. 269-283.

Renard, R.J. and Clarke L.C. 1965. Experiments in numerical objective frontal analysis. *Mon. Wea. Rev.* **93**. 547-556.

Sabo, P., 1992. Application of the thermal front parameter to baroclinic zones around cutoff lows, *Meteorol. Atmos. Phys.*, **47**, 107-115.

Sanders, F. and Doswell, C.A., III. 1995. A case for detailed surface analysis. *Bull. Amer. Meteor. Soc.*, **76**, 505-521.

Saucier, W.J., 1955. Principles of Meteorological Analysis. University of Chicago Press.

Shapiro, M.A. and Keyser, D. 1990. Fronts, Jet Streams and the Tropopause; in 'Extratropical Cyclones, The Erik Palmén Memorial Volume'. American Meteorological Society, Boston. 167-191.

Steinacker, R.A., 1992. Dynamic aspects of frontal analysis, *Meteorol. Atmos. Phys.*, **48**, 93-103.

Thorpe, A.J. 1994. Dynamics of mesoscale sub-structure at fronts. In 'The Life Cycles of Extratropical Cyclones', Proceedings of an international symposium, Bergen, Norway, 27 June - 1 July 1994. vol. I, 220-228. Alma Mater Forlag AS, Bergen.

Young, G.S. and Fritsch, J.M. 1989. A Proposal for General Conventions in Analyses of Mesoscale Boundaries. *Bull. Amer. Meteor. Soc.*, **70**, 1412-1421.

Zwatz-Meise, V. and Bendl, K. 1992. PVA-maxima and their connection to cloud systems in satellite images and to precipitation. *Meteorol. Atmos. Phys.*, **47**, 145-164.

Zwatz-Meise, V. and Hufnagl, F. 1990. Some results about the relation between an objective front parameter and cloud bands in satellite images and its connection to classical cold front models. *Meteorol. Atmos. Phys.*, **42**, 77-89.

Zwatz-Meise, V. and Mahringer, G., 1988. Use of satellite imagery, combined with numerical model diagnostics, to locate fronts and predict their activity: methods and examples. In 'Satellite and radar imagery interpretation' Preprints for a workshop in Reading, England, 20-24 July 1987. Eds: M. Bader and T. Waters. Eumetsat. 143-162.

Zwatz-Meise, V. and Mahringer, G., 1990. SATMOD: An interactive system combining Satellite images and model output parameters. *Weather and Forecasting*, **5**, 233-246.

CURRENT JCMM INTERNAL REPORTS

This series of JCMM Internal Reports, initiated in 1993, contains unpublished reports and also versions of articles submitted for publication. The complete set of Internal Reports is available from the National Meteorological Library on loan, if required.

1. **Research Strategy and Programme**
   K A Browning et al
   January 1993

2. **The GEWEX Cloud System Study (GCSS)**
   GEWEX Cloud System Science Team
   January 1993

3. **Evolution of a mesoscale upper tropospheric vorticity maximum and comma cloud from a cloud-free two dimensional potential vorticity anomaly**
   K A Browning
   January 1993

4. **The Global Energy and Water Cycle**
   K A Browning
   July 1993

5. **Structure of a midlatitude cyclone before occlusion**
   K A Browning and N Roberts
   July 1993

6. **Development in Systems and Tools for Weather Forecasting**
   K A Browning and G Szejwach
   July 1993

7. **Diagnostic study of a narrow cold frontal rainband and severe winds associated with a stratospheric intrusion**
   K A Browning and R Reynolds
   August 1993

8. **Survey of perceived priority issues in the parametrizations of cloud-related processes in GCMs**
   K A Browning
   September 1993

9. **The Effect of Rain on Longwave Radiation**
   I Dharssi
   September 1993

10. **Physical Cloud Microprocesses - A Description of the Parametrization used in the Large Eddy Model**
    H Swann
    July 1994

11. **An Appreciation of the Meteorological Research of Ernst Kleinschmidt**
A J Thorpe
May 1992

12. **Potential Vorticity of Flow Along the Alps**
A J Thorpe, H Volkert and Dietrich Heimann
August 1992

13. **The Representation of Fronts**
A J Thorpe
January 1993

14. **A Parametrization Scheme for Symmetric Instability: Test for an Idealised Flow**
C S Chan and A J Thorpe
February 1993

15. **The Fronts 92 Experiment: a Quicklook Atlas**
Edited by T D Hewson
November 1993

16. **Frontal wave stability during moist deformation frontogenesis**
Part 1. Linear wave dynamics
C H Bishop and A J Thorpe
May 1993

17. **Frontal wave stability during moist deformation frontogenesis**
Part 2. The suppression of non-linear wave development
C H Bishop and A J Thorpe
May 1993

18. **Gravity waves in sheared ducts**
C Bishop and A J Thorpe
November 1993

19. **Potential Vorticity and the Electrostatics Analogy: Quasi-Geostrophic Theory**
C Bishop and A J Thorpe
November 1993

20. **Recent Advances in the Measurement of Precipitation by Radar**
A J Illingworth
April 1993

21. **Micro-Physique et Givrage. Cloud Microphysics and Aircraft Icing**
A J Illingworth
May 1993

22. **Differential Phase Measurements of Precipitation**
M Blackman and A J Illingworth
May 1993

23. **Estimation of Effective Radius of Cloud Particles from the Radar Reflectivity**
N I Fox and A J Illingworth
May 1993

24. **A Simple Method of Dopplerising a Pulsed Magnetron Radar**
A Hau, A J Illingworth and J Eastment
November 1993

25. **Radiation and Polar Lows**
George C Craig
February 1994

26. **Collected preprints submitted to the International Symposium on the Life Cycles of Extratropical Cyclones; Bergen, Norway, 27 June - 1 July 1994**
April 1994

27. **Convective Frontogenesis**
Douglas J Parker and Alan J Thorpe
April 1994

28. **Improved Measurement of the Ice Water Content in Cirrus Using a Total Water Evaporator**
Philip R A Brown and Peter N Francis
April 1994

29. **Mesoscale Effects of a Dry Intrusion within a Vigorous Cyclone**
K A Browning and B W Golding
April 1994

30. **GEWEX Cloud System Study, Science Plan**
May 1994

31. **Parametrization of Momentum Transport by Convectively Generated Gravity Waves**
R Kershaw
February 1995

32. **Mesoscale Modelling Newsletter No 5**
May 1994

33. **Observations of the mesoscale sub-structure in the cold air of a developing frontal cyclone**
K A Browning, S A Clough, C S A Davitt, N M Roberts and T D Hewson
May 1994

34. **Longwave Radiative Forcing of a Simulated Tropical Squall Line**
Imtiaz Dharssi
July 1994

35. **On the nature of the convective circulation at a kata-cold front**
K A Browning
September 1994

36. **Collective preprints of papers submitted to the COST-75 International Seminar on Advanced Weather Radar Systems, Brussels, 20-23 September 1994**
November 1994

37. **Use of satellite imagery to diagnose events leading to frontal thunderstorms: Parts 1 and 11 of a case study**
K A Browning and N M Roberts
November 1994

38. **The role of spaceborne millimetre-wave radar in the global monitoring of ice cloud**
P R A Brown, A J Illingworth, A J Heymsfield, G M McFarquahar, K A Browning and M Gosset
December 1994

39. **Potential Vorticity Inversion**
Michael Ziemianski
October 1994

40. **Theory of mature tropical cyclones; a comparison between Kleinschmidt (1951) and Emanuel (1986)**
Suzanne L Gray
December 1994

41. **Dispersion and removal of pollutants during the passage of an atmospheric frontal system**
N R Gimson
December 1994

42. **The role of snow sublimation in frontogenesis**
D J Parker and A J Thorpe
December 1994

43. **Potential vorticity and the electrostatics Analogy: Ertel-Rossby formulation**
A J Thorpe and C H Bishop
December 1994

44. **Mesoscale aspect of extratropical cyclones: an observational perspective**
K A Browning
January 1995

45. **A Polar Low Outbreak: Evolution and Mesoscale Structures**
T D Hewson, G C Craig and C Claud
February 1995

46. **Generation of near-surface gusts of deep convection**
K Nakamura and R Kershaw
April 1995

47. **Attribution Concepts applied to the Omega Equation**
S A Clough, C S A Davitt and A J Thorpe
June 1995

48. **Parametrization of mixed-phase cloud and precipitation**
Susan P Ballard and M Gerard Hutchinson
June 1995

49. **Short-range forecasting of stratocumulus: Initialization Prediction**
Susan Ballard, Simon D Jackson and B Macpherson
June 1995

50. **Contributions of the JCMM/Dept of Meteorology Radar Group to the 27th AMS Radar Meteorology Conference, Vail October 1995**
June 1995

51. **Cold Pools in Shear**
Douglas J Parker
September 1995

52. **High-resolution analysis of frontal fracture**
K A Browning, S P Ballard and C S A Davitt
September 1995

53. **The Albedo of Broken Cloud Fields: Calculations using a modified two stream radiation code**
Imtiaz Dharssi and Roy Kershaw
October 1995

54. **Parametrization of momentum transport by convection. I: Theory and cloud modelling results**
R Kershaw and D Gregory
November 1995

55. **Variation of frontal structure along a cold front**
K A Browning and N M Roberts
November 1995

56. **Secondary Frontal Waves**
Douglas Parker
December 1995

57. **Objective Fronts**
T D Hewson
March 1996

Met Office Joint Centre for Mesoscale Meteorology Department of Meteorology
University of Reading PO Box 243 Reading RG6 6BB United Kingdom
Tel: +44 (0)118 931 8425 Fax: +44 (0)118 931 8791
www.metoffice.com